Karola, Aaro; Tavakoli, Sasan; Mikkola, Tommi; Matusiak, Jerzy; Hirdaris, Spyros

The influence of wave modelling on the motions of floating bodies

Published in:
Ocean Engineering

DOI:
10.1016/j.oceaneng.2024.118067

Published: 15/08/2024

Document Version
Publisher's PDF, also known as Version of record

Ocean Engineering 306 (2024) 118067

Contents lists available at ScienceDirect

Ocean Engineering

journal homepage: www.elsevier.com/locate/oceaneng

The influence of wave modelling on the motions of floating bodies

Aaro Karola [a,b,*], Sasan Tavakoli [a,c], Tommi Mikkola [a], Jerzy Matusiak [a], Spyros Hirdaris [a,d]

[a] Marine and Arctic Technology Group, Aalto University, Otakaari 4, Espoo, 02150, Finland
[b] Meyer Turku Oy, Turku, Finland
[c] Department of Infrastructure Engineering, The University of Melbourne, Parkville, 3052, VIC, Australia
[d] Global Ship Systems Centre, American Bureau of Shipping, Kalithea, 17674, Athens, Greece

ARTICLE INFO

Keywords:
Wave modelling
Wave-structure interaction
OpenFOAM
Waves2Foam

ABSTRACT

In recent years OpenFOAM studies have focused on pure wave modelling and wave-structure interaction. Considering that there is a lack of transparency concerning effects of different motion modelling settings in OpenFOAM, this paper presents the influence of different numerical setups on the accurate modelling of wave-induced motions. This is achieved by applying the `interFoam` solver included in OpenFOAM-v2206 with the waves2Foam toolbox. The optimal numerical setup is studied with a two-dimensional box-like ship idealisation heaving in varying wave lengths while the wave steepness remains constant. Different numerical setups are considered for accurate wave modelling, the modelling of wave excitation forces for the case of a static structure, and heave motion modelling. Finally, the optimal setup that is found is applied for a 3D ship case in head waves with heave and pitch coupling. As far as practically possible, the results are validated against experimental data. It is shown that strict requirements for mesh density and time step for accurate wave modelling result in accurate excitation force and motion results. Reflections from the relaxation zones and different mesh density layers cause inaccuracies. It is concluded that simple numerical cases are suitable for studying optimal numerical setups for more complex simulation cases.

1. Introduction

In recent years, advances in computational efficiency have enabled the use of Reynolds-Averaged Navier–Stokes-based (RANS) Computational Fluid Dynamics (CFD) methods in ship seakeeping. In comparison to potential flow solvers, RANS CFD solvers apply fewer simplifications in terms of modelling flow physics (e.g. viscosity and turbulence modelling). This allows for more accurate modelling of highly nonlinear effects such as wave breaking and water on decks during stormy sea conditions (Li and Fuhrman, 2022; Lakshmynarayanana and Hirdaris, 2020). Notwithstanding this, RANS methods are sensitive to computational assumptions (e.g. numerical schemes and mesh structure). Problems of application are highlighted in complex modelling cases, such as wave-structure interactions in coastal engineering and naval architecture (Huang et al., 2022).

The first step in replicating seakeeping or wave-structure interactions with CFD is to generate waves in a numerical wave tank (NWT). At first instance, the accuracy of modelling wave-structure interactions is highly dependent on accurate wave modelling. Multiple studies utilising RANS CFD show that accurate wave modelling requires the implementation of a dense mesh close to the free surface, while small time steps are essential during computations (Connell and Cashman, 2016; Roenby et al., 2017; Larsen et al., 2019). Low resolution results in the numerical dissipation of energy, which in turn dampens the modelled wave amplitude. Lower time steps reduce errors in terms of modelling the wave celerity and wave velocity profiles close to the wave crests as compared against theoretical waves (Larsen et al., 2019). Nevertheless, a dense mesh and small time steps may lead to simulations becoming computationally uneconomical, especially in 3D cases.

In addition to accurate wave generation at the wave generation boundary of the computational domain, the waves must also be accurately considered in way of the other fluid domain boundaries. For example, poor absorption of waves at these boundaries leads to waves being reflected. These reflections may affect the generated waves coming from the wave source and the energy of the modelled waves does not leave the computational domain accurately. With this in mind, multiple methods have been developed to model wave absorption. Available modelling choices may involve coarsening the mesh towards the fluid domain boundaries (Yao et al., 2021), beaches that are modelled in the computational domain or considered through numerical

* Corresponding author.
E-mail addresses: aaro.karola@aalto.fi (A. Karola), s.tavakoli@unimelb.edu.au (S. Tavakoli), tommi.mikkola@aalto.fi (T. Mikkola), jerzy.matusiak@aalto.fi (J. Matusiak), spyros.hirdaris@aalto.fi (S. Hirdaris).

https://doi.org/10.1016/j.oceaneng.2024.118067
Received 27 October 2023; Received in revised form 19 April 2024; Accepted 30 April 2024
Available online 10 May 2024

equations (Schmitt et al., 2020), static boundaries (Higuera et al., 2013), and relaxation zone methods (Islam et al., 2019).

The wave inlet boundary is especially problematic with regard to reflections as a dense mesh must be implemented from the wave source to a structure. Thus, numerical beaches or mesh coarsening towards the inlet boundary cannot be applied. Reflected waves from the structure or other fluid domain boundaries reaching the inlet could be re-reflected and disturb the wave generation that is applied. One solution is to stop the simulation before reflected waves reach the wave source boundary (Devolder et al., 2017). However, reaching steady state or quasi-static conditions during the simulation may require long simulation times. Numerical damping methods, such as relaxation zones, are often the preferred choices. A relaxation zone can be placed in front of the wave-generating boundary. This ensures that the waves have the desired height at a prescribed distance from this boundary (Jacobsen et al., 2012a).

Another important step in modelling wave-structure interactions with CFD is the consideration of dynamic mesh motions. These refer to solving the rigid body motions and updating the mesh structure with the new position of the body (Huang et al., 2022). The computation of rigid body motions includes different relaxation and damping parameters (OpenFOAM, 2023). No clear explanation for the application of these parameters exists in the literature. Different methods exist for updating the mesh, such as mesh-morphing and overset methods. The former is preferred in small motions without a wave-induced drift effect. The main challenge with mesh-morphing is the specification of the extent of the distorted mesh. The latter method is generally applied for large-amplitude motions. The main difficulty is the interpolation in between a background mesh and an overset region which introduces errors to all fluid fields (velocity, pressure, and fluid fraction) (Chen et al., 2019; Tavakoli et al., 2021).

Currently, pure wave modelling in OpenFOAM-related research is separated from the wave-structure interaction studies. The results from pure wave modelling studies for accurate wave modelling are not applied in wave-structure interaction studies. Additionally, there are no studies that transparently present the effect of the numerical setup in OpenFOAM for wave-structure interaction modelling. Therefore, this paper aims to unite pure wave modelling and wave-structure interactions in OpenFOAM with transparent presentation of the whole numerical setup and their effect for accurate wave-structure interaction studies. The modelled test case of a box-like 2D ship idealisation in regular waves with an allowance for heave only is studied to find the optimal numerical setup for wave-structure interactions. This simple flow case was selected for two reasons. The first one is the fact that experimental results are available for the case. The second reason is the simplicity of the case, which allows an in-depth study of the appropriate way of wave modelling that considers reflections from the computational domain boundaries and from the structure being investigated. The lessons learned from these are then applied in a complex 3D wave-structure interaction problem of a RoPax ship in head waves while allowing heave and pitch coupling.

The OpenFOAM-v2206 (OpenFOAM, 2023) with waves2Foam toolbox (Jacobsen et al., 2012a) is applied for the numerical simulations. All the steps of wave-induced motion modelling, i.e. waves, excitation forces on a static structure, and motions, are presented and compared against the available experiments. The results from the experimental studies by Rodríguez and Spinneken (2016) are used to validate the numerical results for the 2D box case. The experimental results from Kukkanen and Matusiak (2014) are used to validate the numerical results for the 3D RoPax ship case. The paper starts with state-of-the-art research in ship seakeeping with RANS CFD using OpenFOAM (see Section 2). The fundamental theory of RANS CFD modelling for wave-structure interactions and a detailed description of the numerical methods applied and study cases are presented in Sections 3, 4, and 5. The results are introduced in Section 6 and further discussion is presented in Section 7.

2. Literature survey

Ship seakeeping studies started in the 1950s with Korvin-Kroukovsky et al. who studied the heaving and pitching motions using a strip theory-based potential flow solver (Korvin-Kroukovsky and Jacobs, 1957). Salvesen et al. (1970) published their version of the strip theory in 1970s. The strip theory method assumes that a ship hull can be modelled with 2D cross-sections; thus, it is suitable for slender hulls. Fully three-dimensional panel methods were first published in the late 1970s and early 1980s by Chang (1977), Inglis and Price (1980), and Guevel and Bougis (1982). Initially, strip and panel methods were developed in the frequency domain and later in the time domain (Yamamoto et al., 1978; Liapis, 1985). Frequency domain codes assume linearity by considering wave and motion amplitudes to be small. Linear methods are fast and often accurate enough (Karola et al., 2022). Time domain codes may include some nonlinear effects by regarding the actual wave elevation on the hull surface or the large-amplitude motions often increasing in terms of accuracy even in extreme wave conditions (Kukkanen and Matusiak, 2014). Today, potential flow theory with strip and panel methods is still applied (Parunov et al., 2022; Show et al., 2022). This is because it is numerically economical and the related hydrodynamic assumptions are well understood.

Potential flow theory cannot model viscosity or highly nonlinear phenomena such as turbulence or breaking waves without the introduction of artificial terms. RANS solvers can overcome these limitations. The first studies to apply RANS solvers for ship hydrodynamics were published in the 1980s and these focused on ship resistance and flow around the hull (Miyata et al., 1985; Kodama, 1985). During the 1990s, RANS solvers were first applied to idealise ship motions during manoeuvring. The results were promising, especially with regard to modelling the flow around the hull and the prediction of exciting forces and moments (Akimoto, 1997; Ohmori, 1998; Takada et al., 1998). In 1999, Sato et al. published a study of the heave and pitch motions of a ship in regular waves using a RANS solver (Sato et al., 1999).

In the early 2000s, most RANS studies applied in-house software codes (Hochbaum and Vogt, 2002; Orihara and Miyata, 2003; Weymouth et al., 2005). Since the 2010s, the application of general-purpose commercial CFD software codes in seakeeping research has become popular. Examples are the ISIS-CFD (Queutey and Visonneau, 2007; Hänninen et al., 2012; Bekhit and Lungu, 2019), Star-CCM+ (Kim, 2011; Tezdogan et al., 2015; Chowdhury et al., 2023), and ANSYS Fluent (Grasso et al., 2010; Yan et al., 2015; Acharya et al., 2023) commercial solvers. In recent years, research using OpenFOAM-based CFD has gained popularity in academic research. Accordingly, many seakeeping studies applying RANS solvers in OpenFOAM have been published recently (Löhrmann and Hochbaum, 2014; Gao et al., 2021; Sulovsky et al., 2023). In general, the studies show that RANS solvers have good accuracy in modelling ship motions and excitation forces. However, attention must be paid to meshing. Additionally, RANS solvers have a much higher computational cost than potential flow solvers.

RANS solvers aim to model waves accurately by generating them at the wave source and then propagating them throughout the computational domain. At the wave source, the generated waves are generally based on potential flow theory, such as the 5th-order Stokes (De, 1955), or stream function theories (Rienecker and Fenton, 1981). The modelling of free-surface flows inside the fluid domain can be divided into Lagrangean and Eulerian methods (Rakhsha et al., 2021). The former, e.g. the Smoothed Particle Hydrodynamics (SPH) (Gingold and Monaghan, 1977) and Moving Particle Semi-implicit (MPS) (Koshizuka and Oka, 1996) techniques, are meshless methods in which the fluid motions are modelled in the form of moving particles. Eulerian methods apply a mesh to model the fluid flow and can be further categorised into surface tracking and surface capturing methods. The difference between these two is whether the mesh is updated on the basis of waves (surface tracking) or not (surface capturing) and whether the governing equations are solved only for the water phase (surface tracking) or also for the air phase (surface capturing) (Farmer et al., 1994; Tahara and Stern, 1996; Li et al., 2001; Hirt and Nichols, 1981). The currently popular Volume Of Fluid (VOF) method is an example of a surface capturing method (Hirt and Nichols, 1981). Lagrangian methods can model highly nonlinear phenomena, such as wave breaking, more accurately than Eulerian methods. However, Eulerian methods model pressure fields more accurately and are more robust (Garoosi et al., 2022; Rakhsha et al., 2021). When one compares surface tracking and capturing methods, surface tracking methods are more accurate and have a lower computational cost but they cannot model highly distorted free surface profiles. On the other hand, surface capturing methods require particular care in terms of the discretisation of the free surface (Armenio, 1998; Rhee and Stern, 2001).

Wave modelling with OpenFOAM started in the early 2010s, when Afshar and Morgan et al. implemented versions for the generation of Stokes waves at the wave source and applying VOF in the fluid domain (Afshar, 2010; Morgan et al., 2011). Jacobsen et al. improved both of these methods in the first version of the waves2Foam toolbox (Jacobsen et al., 2012a,b) and Higuera et al. published a wave modelling tool known as IHFoam (Higuera et al., 2013). Both tools can model various wave types. However, the waves2Foam solver applies a relaxation zone method to absorb waves in the way of the fluid domain boundaries, while the IHFoam solver applies shallow water theory. IHFoam is implemented in the newest versions of OpenFOAM, while waves2Foam needs separate installation (OpenFOAM, 2023; Jacobsen et al., 2012a). OpenFOAM with the waves2Foam toolbox has been applied extensively for various cases in recent years, such as payloads (Yan et al., 2020), overtopping against dikes (Chen et al., 2021), and hydroelastic studies of a container ship (Wei and Tezdogan, 2022).

In OpenFOAM, the generally applied solver for free surface flows, namely `interFoam`, applies the VOF method with the MULES (MUltidimensional Limiter for Explicit Solution) algorithm for solving the location of the free surface (OpenFOAM, 2023; Deshpande et al., 2012; Damián and Nigro, 2014). However, the MULES algorithm may introduce spurious velocities close to the water and air interface, which causes wiggles in the modelled free surface (Vukčević et al., 2017). Different algorithms have been developed to correct this problem, such as isoAdvector and the Ghost Fluid Method (GFM) (Vukčević et al., 2017; Roenby et al., 2016). The former is included in the newest OpenFOAM versions (since OpenFOAM-v1706) as an `interFlow` solver (OpenFOAM, 2023). Various parametric studies have shown that, compared to `interFoam`, `interFlow` has demonstrated a sharper free surface and less sensitivity to the cell aspect ratio (Roenby et al., 2017; Larsen et al., 2019). However, the application of `interFlow` with a moving structure may introduce air bubbles into the water phase close to the structure, which reduces the accuracy of motion modelling in comparison to an `interFoam` solver (Decorte et al., 2019). On this basis an `interFoam` solver may be considered to be a better choice for wave-structure studies.

The absorption of waves at domain boundaries has been studied for some time. In the 1970s, Orlanski presented a boundary condition to absorb reflections (Orlanski, 1976). In the 1980s, Madsen et al. presented a study in which they applied a permeable structure to absorb waves (Madsen, 1983). In the 1990s, Mayer presented a relaxation method to reduce wave reflections from the domain boundaries (Mayer et al., 1998). The Waves2Foam toolbox applies a relaxation zone method based on Mayer (Jacobsen et al., 2012a). Relaxation zone methods require an increase in domain sizes; thus, IHFoam applies a static boundary method based on shallow water theory (Higuera et al., 2013). Windt et al. carried out an extensive study of the different methods that absorb waves close to boundaries. The methods they compared were a relaxation zone, static and dynamic boundaries, numerical or sloped beach, and mesh coarsening methods. Each method offers benefits, depending on the wave conditions, but the relaxation zone method was shown to have good overall performance (Windt et al., 2019). Similar results were observed by Conde, who compared wave absorption methods with waves2Foam and IHFoam (Conde, 2019). On the basis of these experiences, the waves2Foam toolbox is applied in this paper.

The motions of structures can be modelled by a morphing-mesh or an overset method. The former evolves the mesh on the basis of the motion of structures. The latter applies multiple overlapping constant subdomains which communicate with each other. Both methods have been studied since the 1980s (Benek et al., 1986). OpenFOAM includes both morphing-mesh and overset methods for dynamic mesh analysis, both of which have been extensively studied (Huang et al., 2022; OpenFOAM, 2023). Palm et al. applied a mesh-morphing method in their study of wave energy converters (Palm et al., 2016). Similarly, Islam et al. applied a mesh-morphing method in their study of wave radiation by a box structure (Islam et al., 2019). In both studies, the simulation results matched the experimental data. Tavakoli et al. applied an overset method to study green water effects for floating bodies (Tavakoli et al., 2021). Windt et al. validated their numerical wave tank which applied an overset method against experiments (Windt et al., 2020). Chen et al. compared mesh-morphing and overset methods for various dynamic mesh cases (Chen et al., 2019). These published papers show that overset is a favourable option in large-amplitude motions, but in small-amplitude motions mesh-morphing is more efficient. Moreover, there is a lack of transparency regarding how the dynamic motion libraries are applied. In this paper, small-amplitude motions are studied; thus, a mesh-morphing method is applied.

3. Theory

The governing equations in CFD analyses are the Navier–Stokes (NS) and continuity equations (el Moctar et al., 2021). In RANS modelling, the NS equation for an incompressible fluid is expressed as

$$\frac{\partial u_i}{\partial t} + u_j \frac{\partial u_i}{\partial x_j} = -\frac{1}{\rho}\frac{\partial p}{\partial x_i} + \frac{\partial}{\partial x_j}((\nu + \nu_t)\frac{\partial u_i}{\partial x_j}) + g_i, \tag{1}$$

where u_i and u_j are the time-averaged velocity, t is time, x_i is the coordinate axis direction, ρ is the fluid density, p is the time-averaged pressure, ν is the kinematic viscosity of the fluid, and ν_t is the turbulent eddy kinematic viscosity, which is zero in laminar flow cases. g_i is the gravitational acceleration. The continuity equation for incompressible fluids is

$$\frac{\partial u_i}{\partial x_i} = 0. \tag{2}$$

In the Volume of Fluid (VOF) method each cell in the computational domain is defined with the volume fraction of water, α, where $\alpha = 1$ defines the cell being filled with water and $\alpha = 0$ full of air (OpenFOAM, 2023). Thus, the free surface is defined to be where $\alpha = 0.5$. The transport equation is applied to transport the volume fraction inside the computational domain:

$$\frac{\partial \alpha}{\partial t} + \frac{\partial \alpha u_i}{\partial x_i} = 0. \tag{3}$$

The waves applied in this research are regular Stokes II waves. Therefore, the wave elevation, η, is modelled as

$$\eta(x,t) = \frac{H}{2} cos(kx - \omega_w t + \phi) + \frac{H^2 k}{16}\frac{cosh(kh)}{sinh^3(kh)} \times (2 + cosh(2kh)) cos(2(kx - \omega_w t + \phi)), \tag{4}$$

where H, k, ω_w and ϕ are the wave height, wave number, wave angular frequency, and phase shift respectively. h is the water depth. The wave velocity in 2D cases is modelled as

$$u = \frac{Hgk}{2\omega_w}\frac{cosh(k(h+z))}{cosh(kh)} cos(kx - \omega_w t + \phi) + \frac{3H^2\omega_w k}{16}\frac{cosh(2k(h+z))}{sinh^4(kh)} cos(2(kx - \omega_w t + \phi)), \tag{5}$$

$$w = \frac{Hgk}{2\omega_w}\frac{sinh(k(h+z))}{cosh(kh)}sin(kx-\omega_w t+\phi) + \frac{3H^2\omega_w k}{16}\frac{sinh(2k(h+z))}{sinh^4(kh)}sin(2(kx-\omega_w t+\phi)), \quad (6)$$

where z represents the vertical coordinate location relative to the still water level (Lin, 2008).

For a $k-\omega$ SST turbulence model the eddy viscosity, $\mu_t = \rho\nu_t$, is modelled with the turbulent kinetic energy, k, and turbulent specific dissipation, ω. Consequently, turbulence effects are solved as follows:

$$\frac{\partial(\rho k)}{\partial t} + \frac{\partial(\rho u_j k)}{\partial x_j} = P - \beta^*\rho\omega k + \frac{\partial}{\partial x_j}[(\mu+\sigma_k\mu_t)\frac{\partial k}{\partial x_j}], \quad (7)$$

$$\frac{\partial(\rho\omega)}{\partial t} + \frac{\partial(\rho u_j\omega)}{\partial x_j} = \frac{\gamma}{\nu_t}P - \beta\rho\omega^2 + \frac{\partial}{\partial x_j}[(\mu+\sigma_\omega\mu_t)\frac{\partial\omega}{\partial x_j}] + 2(1-F_1)\frac{\rho\sigma_{\omega 2}}{\omega}\frac{\partial k}{\partial x_j}\frac{\partial\omega}{\partial x_j}, \quad (8)$$

where

$$P = \tau_{ij}\frac{\partial u_i}{\partial x_j}, \quad (9)$$

$$\tau_{ij} = \mu_t(2S_{ij} - \frac{2}{3}\frac{\partial u_k}{\partial x_k}\delta_{ij}) - \frac{2}{3}\rho k\delta_{ij}, \quad (10)$$

$$S_{ij} = \frac{1}{2}(\frac{\partial u_i}{\partial x_j} + \frac{\partial u_j}{\partial x_i}). \quad (11)$$

Finally, the turbulent eddy viscosity can be solved as

$$\mu_t = \frac{\rho a_1 k}{max(a_1\omega, \Omega F_2)}, \quad (12)$$

where μ is the dynamic viscosity of the fluid, the terms β, σ, γ, and a_1 are constants, and F_1, F_2, and Ω are additional factors. Details of the above are discussed in the OpenFOAM user guide and its OpenFOAM (2023), Menter and Esch (2001) and Menter et al. (2003).

The waves2Foam toolbox uses relaxation zones to absorb waves in unwanted directions. Inside the relaxation zone, the computational variable ϕ, which can be either α or u_i, is corrected by a weighted sum:

$$\phi = (1-\omega_R)\phi_{target} + \omega_R\phi_{computed}, \quad (13)$$

where ϕ_{target} is the theoretical value from the Stokes theory and $\phi_{computed}$ is the simulated value; $\omega_R \in [0,1]$ is the weighting function, which is a function of the local coordinate inside the relaxation zone (Jacobsen et al., 2012a).

If motions are accounted for, the total force on the floating body is computed by integrating the pressure over its surface. Then the acceleration is calculated according to Newton's second law of motion as

$$F_i = ma_i \quad (14)$$

where F_i is the total force on the floating body, m is the mass of the structure, and a_i is the acceleration (OpenFOAM, 2023).

4. Numerical methods

Numerical methods aim for the accurate idealisation of the wave propagation throughout the computational domain. The goal is to achieve accurate modelling of the wave excitation forces and motions. Accurate wave modelling was studied by Larsen et al.; thus, the numerical schemes applied in this paper mostly follow their results (Larsen et al., 2019). The numerical setup that was applied (`Setup1`) is presented in Table 1 for laminar wave modelling cases. In OpenFOAM, the `CrankNicolson` time scheme is a combination of the Crank–Nicolson and implicit Euler discretisation schemes. The factor of 1 corresponds to a pure Crank–Nicolson scheme and the factor of 0 to a pure implicit Euler scheme. The combination of a `CrankNicolson` time scheme with a factor of 0.3 and the `upwind` scheme for the convection terms is considered sufficient to model stable wave propagation (Larsen et al., 2019). With one outer corrector (`nOuterCorrectors = 1`) the transport equation for the volume fraction (Eq. (3)) is solved only once for each time step (see Fig. 1). This means that the velocity in the transport equation corresponds to the value from the previous time step introducing a partly explicit character to the equation.

Table 1
Main numerical setup (`Setup1`) for the simulations with OpenFOAM terminology.

`ddtSchemes`	`CrankNicolson 0.3`
`gradSchemes`	`Gauss linear`
`divSchemes`	
`div(rhoPhi,U)`	`Gauss upwind`
`div(phi,alpha)`	`Gauss vanLeer`
`div(phirb,alpha)`	`Gauss interfaceCompression`
`laplacianSchemes`	`Gauss linear corrected`
`interpolationSchemes`	`linear`
`snGradSchemes`	`corrected`
PIMPLE settings	
`nOuterCorrectors`	1
`nCorrectors`	2
`nNonOrthogonalCorrectors`	1
Turbulence modelling	laminar
waves2Foam settings	
Relaxation zone shape	`rectangular`
Relaxation zone weight	`exponential` (Jacobsen et al., 2012a)

In many publications waves are modelled with laminar solvers (Connell and Cashman, 2016; Roenby et al., 2017; Larsen et al., 2019). Thus, the effect of turbulence modelling on waves is also studied with the $k-\omega$ SST model. Additionally, the effect of the numerical setup is studied by changing some of the numerical schemes, with their difference outlined in Table 2. The `limitedLinearV` scheme is less diffusive in comparison with the `upwind` scheme and the pure Crank–Nicolson time scheme is less diffusive than the implicit Euler time scheme. Therefore, the schemes in `Setup2` - `Setup4` are less diffusive than in `Setup1`. Accordingly, multiple `nOuterCorrectors` aim to balance the possible instabilities caused by lower diffusion. Similarly to `Setup1`, `Setup2` was shown to produce a stable wave by Larsen et al. (2019).

The time step during the simulations is controlled by the Courant number, defined as

$$Co = \Delta t\frac{\sum_{faces}|\Phi_i|}{2V}, \quad (15)$$

where Δt is a time step, Φ_i is the face volumetric flux in the different coordinate directions, and V is the cell volume. In all cases, the maximum Courant number is set to be 0.3 to achieve a balance between small enough time steps and fast simulation times (Larsen et al., 2019). A constant maximum Courant number in all of the cases guarantees a smaller time step in more dense meshes.

OpenFOAM's `interFoam` solver for two-phase flows applies the MULES algorithm, where an additional compression term is included into the transport equation for volume fraction α (see Eq. (3)) to achieve a sharper interface between the two fluids:

$$\frac{\partial\alpha}{\partial t} + \frac{\partial\alpha u_i}{\partial x_i} + \frac{\partial}{\partial x_i}(\alpha(1-\alpha)u_i^r) = 0. \quad (16)$$

In Eq. (16) u_i^r is modelled as the relative velocity across the fluid interface. The governing equations are solved with OpenFOAM's PIMPLE algorithm, which is a combination of the SIMPLE (Semi-Implicit Method for Pressure Linked Equations) and PISO (Pressure-Implicit with Splitting of Operators) algorithms (OpenFOAM, 2023; Caretto et al., 1973; Issa, 1986). A simplified solving procedure is shown in Fig. 1 (Jasak, 1996).

The motion of a structure can be controlled by two factors: `accelerationRelaxation` ($R_a \in [0,1]$) and `accelerationDamping`

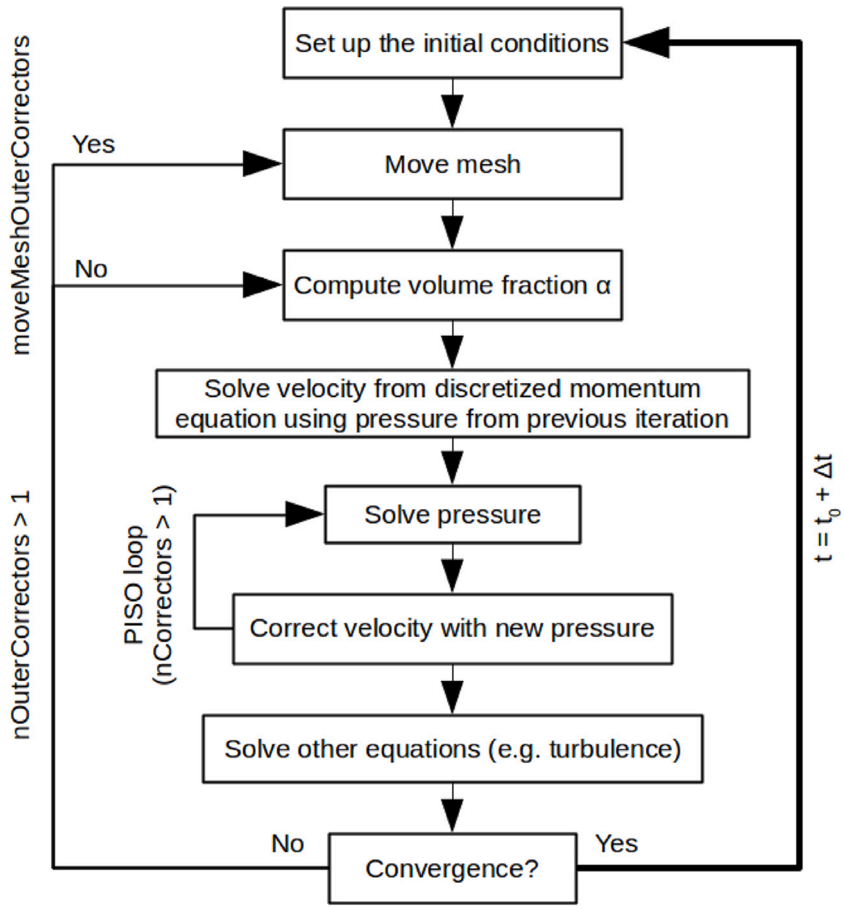

Fig. 1. Simplified procedure in the PIMPLE algorithm.

Table 2
Differences between the numerical setups that were compared to `Setup1` (see Table 1).

`Setup2`	
`ddtSchemes`	`CrankNicolson 0.625`
`div(rhoPhi,U)`	`Gauss limitedLinearV 1`
`nOuterCorrectors`	`2`
`Setup3`	
`ddtSchemes`	`CrankNicolson 0.625`
`div(rhoPhi,U)`	`Gauss limitedLinearV 1`
`nOuterCorrectors`	`8`
`Setup4`	
`ddtSchemes`	`CrankNicolson 0.625`
`div(rhoPhi,U)`	`Gauss limitedLinearV 1`
`nOuterCorrectors`	`8`
`div(phi,k)`	`Gauss linearUpwind limitedGrad`
`div(phi,omega)`	`Gauss linearUpwind limitedGrad`
Turbulence modelling	$k-\omega$ SST

($D_a \in [0,1]$). R_a is applied to relax the computed acceleration of the structure at each time step:

$$a = R_a a_1 + (1 - R_a) a_0, \tag{17}$$

where a is the relaxed acceleration, a_1 is the acceleration computed with Eq. (14) at the current time step, and a_0 is the relaxed acceleration from the previous time step.

The consideration of D_a varies slightly with the motions solver that is applied. OpenFOAM offers three options for motions solvers, namely Newmark (Newmark, 1959), Crank–Nicolson (Crank and Nicolson, 1947), and symplectic (Dullweber et al., 1997). The computations of motions by each solver are demonstrated in Fig. 2. The velocity is updated in a similar fashion with the Newmark and Crank–Nicolson solvers, but the position of the centre of gravity (COG) is updated differently. On the other hand, the symplectic solver first updates the velocity with the acceleration from a previous time step and applies this velocity to correct the COG. After this, the acceleration is updated and the velocity is corrected by a new acceleration.

The application of a mesh-morphing method introduces distance parameters (`innerDistance` and `outerDistance` in OpenFOAM terminology) to control the morphing distance of the mesh from the structure. `innerDistance` is the smaller value of these two and describes the distance from the structure inside which the mesh is moved as a rigid body. `outerDistance` controls the distance from the structure further than which the mesh is not morphed. Accordingly, the mesh is morphed between these two defined distances.

5. Case study

The study case for steps 1–4 in Table 3 is similar to the one used in the experiments of Rodríguez and Spinneken (2016), who worked on a static and heaving box-like structure with a beam $2b = 0.5$ m and draft of $d = b$ floating in a wave tank of a depth $h = 1.25$ m. Accordingly, this paper studies excitation forces on a static 2D box and motion amplitudes for pure heave motion and explains the principles of wave, force, and motions modelling. After this, the optimal numerical setup that was found is applied in a more complex case of the 3D simulation of a RoPax ship in waves previously studied by Kukkanen and Matusiak (2014) (see Table 3). In the following sections, wave modelling is initially studied in the 2D NWT without any structure. Nonlinear forces and motions are consequently studied for the case of a 2D static box and a box in pure heaving motion and the results are compared against the results obtained by Rodríguez and Spinneken

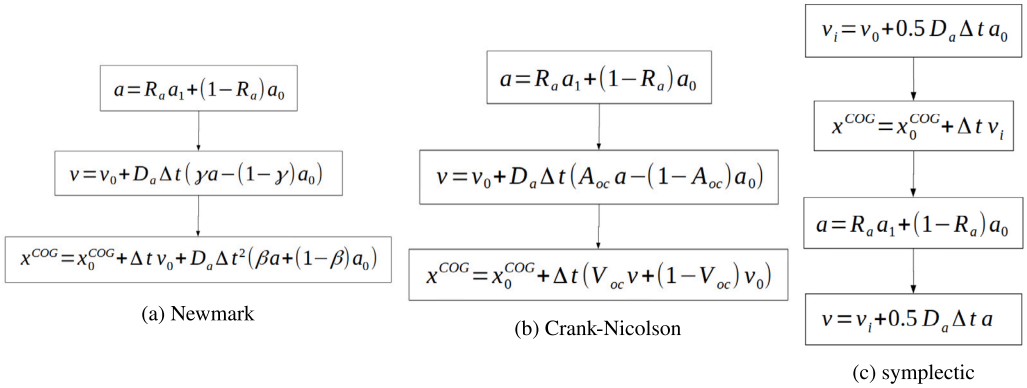

Fig. 2. Computation of motions in Newmark, Crank–Nicolson, and symplectic solvers; v, v_0, x^{COG} and x_0^{COG} respectively represent the velocity and location of the COG of the structure at different time steps; v_i is the initially computed velocity in the symplectic solver; γ, β, A_{oc} and V_{oc} are constant terms embedded in the Newmark and Crank–Nicolson solvers.

Table 3
Modelling and simulation steps.

Step	Objective and description	Assumptions
1	Accurate wave modelling. The influence of numerical schemes, mesh, and mesh aspect ratio are studied.	Denser mesh and lower mesh aspect ratio improves wave modelling. Less diffusive schemes and a larger number of outer correctors lead to improved predictions.
2	Verification and validation of the numerical setup for heave excitations.	The setups producing the most accurate wave modelling produce the most accurate prediction of the excitation force. A larger `nOuterCorrector` improves the results.
3	Motion modelling in OpenFOAM.	Motion solver and acceleration relaxation and damping terms affect motions significantly.
4	Verification and validation of the numerical wave and motion setups for heave motions.	Numerical setup is accurate in prediction of heave RAOs. A larger `nOuterCorrector` improves the results.
5	Application of the optimal setup in the 3D simulation case of a RoPax ship in waves	Accurate setup in 2D is also accurate for 3D simulations

Table 4
Wave modelling study cases.

kb	k [1/m]	λ [m]	ω_w [1/s]	T [s]	H [m] ($ka = 0.05$)	H [m] ($ka = 0.1$)
0.2	0.8	7.85	2.44	2.57	0.13	0.25
0.4	1.6	3.93	3.89	1.62	0.06	0.13
0.5	2.0	3.14	4.40	1.43	0.05	0.10
0.7	2.8	2.24	5.24	1.20	0.04	0.07
1.0	4.0	1.57	6.26	1.00	0.03	0.05
1.2	4.8	1.31	6.86	0.92	0.02	0.04

(2016). The length of the NWT varies according to the wavelength. A wide range of wave lengths is applied to study the excitation forces and heave motions in short and long waves. Two wave steepnesses, $ka = 0.05$ and $ka = 0.1$, are studied to gain an understanding of the effects of steep waves on hydrodynamic response (see Table 4). Finally, 3D simulation with the RoPax ship is performed with three wave lengths and two wave heights.

5.1. Wave modelling

The results from the longest ($kb = 0.2$) and the shortest ($kb = 1.2$) wave cases with both wave steepnesses are demonstrated (see Table 4). The domain length is set to be eight wave lengths long, with relaxation zones one wave length long at the inlet and outlet sides to absorb waves and reflections. Three wave probes (P1, P2, and P3) are applied to measure the wave amplitude throughout the domain. The computational domain is presented in Fig. 3.

At the inlet and outlet boundaries, the waves2Foam toolbox controls the boundary conditions for the volume fraction, pressure, and velocity on the basis of the modelling of the Stokes II wave at the inlet and absorption of the waves at the outlet. At the bottom boundary, wall conditions are applied; thus, the velocity is set to be zero, the pressure gradient is set so that the specified flux is achieved, and a zero gradient condition is applied for volume fraction. At the top boundary, atmospheric conditions are modelled. Hence the pressure is assumed to be zero. The conditions for volume fraction and velocity vary between a zero gradient for outflow through the boundary and a constant flow for inflow through the boundary. For turbulence modelling, constant values are applied at the inlet boundary for k, ω, and v_t on the basis of the NASA Turbulence Modelling Resource (NASA, 2023). At the outlet and top boundaries, the conditions for k and ω vary between a zero gradient and constant flow, depending on the outflow and inflow, respectively, and a zero gradient condition is applied for v_t. Wall functions are applied at the bottom boundary. Table 5 summarises the

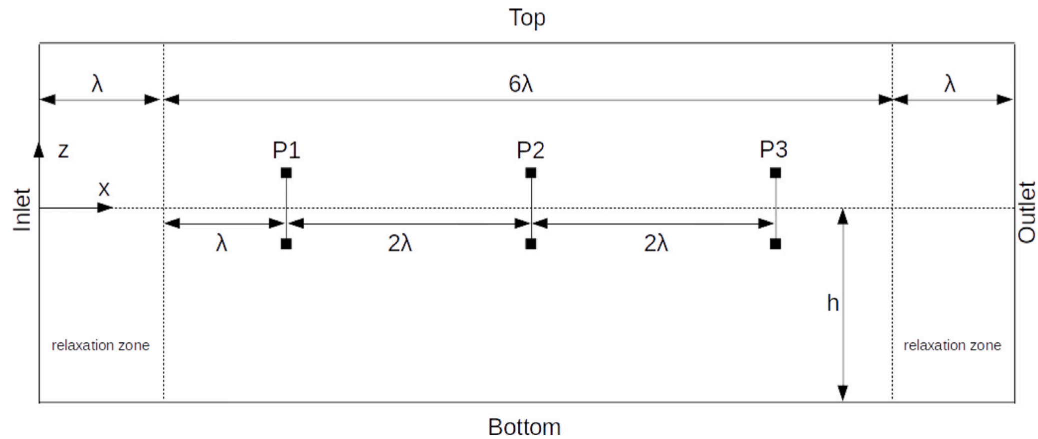

Fig. 3. Computational domain applied for wave modelling study.

Table 5
The boundary conditions applied in OpenFOAM terminology.

	Inlet	Outlet	Top	Bottom
α	zeroGradient	zeroGradient	inletOutlet	zeroGradient
U	zeroGradient	fixedValue	pressureInletOutletVelocity	fixedValue
p_{rgh}	zeroGradient	zeroGradient	totalPressure	fixedFluxPressure
k	fixedValue	inletOutlet	inletOutlet	kqRWallFunction
ω	fixedValue	inletOutlet	inletOutlet	omegaWallFunction
ν_t	fixedValue	zeroGradient	zeroGradient	nutkRoughWallFunction

Table 6
Constant terms.

Term	value
ρ_{air}	1.2 kg/m^3
ν_{air}	1.45 $\times 10^{-5}$ m^2/s
ρ_{water}	1000
ν_{water}	1.0 $\times 10^{-6}$ m^2/s
g	9.81 m/s^2

boundary conditions in OpenFOAM terminology and Table 6 shows the constant terms used during the simulation. Each simulation starts from still water conditions in which the volume fraction is set to be 1 below the free water surface, velocities are zero, and hydrostatic pressure is only considered. The initial values used to idealise the effects of turbulence (k, ω, and ν_t) are based on the NASA Turbulence Modelling Resource (NASA, 2023).

According to previous studies, the number of cells per wave height ($H/\Delta z$) is an important factor in comparison to that of cells per wave length. This is because the application of enough cells per wave height in combination with the small mesh aspect ratio causes cells also to be small in the wave length direction and satisfies the requirement for cells per wave length (Connell and Cashman, 2016; Roenby et al., 2017; Larsen et al., 2019). Generally, at least $H/\Delta z = 10$ is recommended; thus, in this paper the number of cells is varied between $5, 10, 15$, and 20 cells per wave height. Previous studies also recommend applying an aspect ratio of one ($AR = 1$) (Roenby et al., 2017; Jacobsen et al., 2012b). However, because a small aspect ratio would require a very large number of cells in large 3D cases, the initial mesh density comparison is performed with $AR = 1$ and then the effect of a larger aspect ratio is studied with $AR = 1, 2, 4, 8$.

In OpenFOAM, the mesh is initially generated with the `blockMesh` algorithm, which generates a structured mesh (see Fig. 4). Consequently, the mesh is refined in defined areas by using the `refineMesh` tool to achieve dense areas around the still water level for accurate wave modelling and a coarser mesh further away from the still water level to reduce the number of cells. The height of the dense area is one wave height to both sides of the still water level. Along the x-coordinate direction, the mesh stays constant until the wave probe P3. After this point the mesh is gradually coarsened towards the outlet boundary by doubling the cell size. The mesh is coarsened towards the outlet boundary to dampen the wave more effectively with the relaxation zone and to reduce the number of cells.

5.2. Accurate prediction of forces

The accuracy of the setup is tested for excitation force modelling in the case of a static box (see Fig. 5). Three wave cases are modelled ($kb = 0.4, 0.7, 1.0$ and $ka = 0.1$; see Table 4) and the results are compared against experiments (Rodríguez and Spinneken, 2016). The box is located at the centre of the domain in the x-direction and the inlet and outlet boundaries are located three wave lengths away from the box with relaxation zones one wave length long at both ends. This setup achieves efficient absorption of reflections in the shortest domain, and it is therefore computationally efficient (Karola et al., 2023). Two wave probes (P1 and P2) are applied to decompose the measured wave into incoming and reflected wave components according to the method of Goda and Suzuki (1976).

The same boundary and initial conditions as in the wave modelling study are applied (see Tables 5 and 6). The same wall boundary conditions are used for the box structure as on the bottom boundary (see Tables 5 and 6). In OpenFOAM, the box structure is modelled with the `snappyHexMesh` tool after the background mesh is created. For the background mesh a similar setup is applied as in the wave modelling cases, with some additional refining of the mesh around the box (see Fig. 6). The excitation forces on the box are recorded with the `forces` library in OpenFOAM (OpenFOAM, 2023).

5.3. Motion modelling

After the accuracy of the setup for excitation force modelling has been confirmed, the static box is assumed to heave and the accurate numerical setup for motion modelling is studied. This study is performed

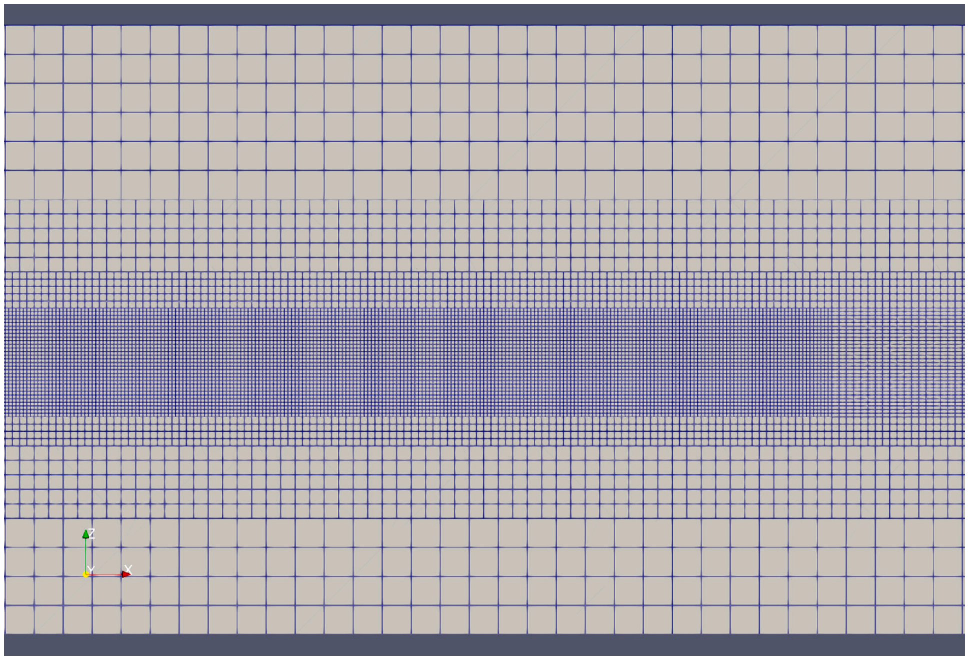

Fig. 4. An example of a computational mesh for the case $H/\Delta z = 15$ and $AR = 1$. Towards the inlet the mesh stays constant and further coarsening is applied towards the outlet direction. In the vertical direction the cell size doubles in the x- and z-directions at each coarsening step.

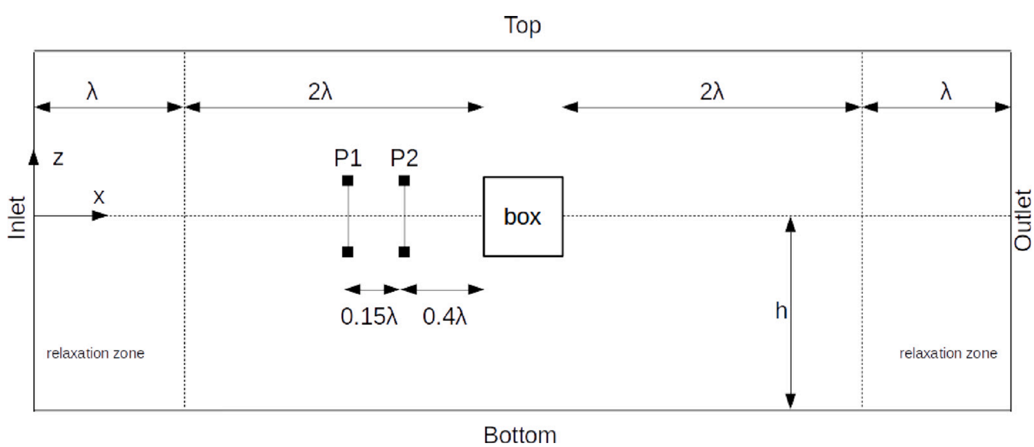

Fig. 5. Computational domain applied for excitation force modelling.

for $kb = 0.5$, which corresponds to the resonance frequency for the heave motion (Rodríguez and Spinneken, 2016). The same domain is applied as shown in Fig. 5. The boundary condition for the velocity of the box is changed from a constant value of zero to a constant value based on the velocity of the box (`movingWallVelocity` in OpenFOAM). The velocity of the box is defined at each time step by OpenFOAM's dynamic motion library.

Accurate heave motion modelling is studied by comparing the three motion solvers (see Fig. 2) with constant values for acceleration relaxation (R_a) and damping (D_a) terms. Next, the effect of the values of the factors R_a and D_a are studied with a Newmark solver by varying each of these parameters between 0.3 and 0.99 while keeping the other constant. The mesh morphing distance parameters (`innerDistance` and `outerDistance` in OpenFOAM) were also studied. However, these did not affect the motion amplitudes. Therefore, constant values of `innerDistance` = 0.05 and `outerDistance` = 0.75 were applied in all the results that are presented. These values roughly correspond to the expected motion amplitude and 15 times the expected amplitude in the case of $kb = 0.5$ with $ka = 0.1$. The setup values are validated against experiments (Rodríguez and Spinneken, 2016). Finally, all the wave conditions presented in Table 4 are applied to compute the heave motion RAOs, which are compared against experiments (Rodríguez and Spinneken, 2016).

5.4. 3D modelling case with a ship hull

The optimal numerical setup is verified in a more complex simulation case by applying it in a 3D case of a ship hull in waves. The case is the same as previously studied by Kukkanen and Matusiak (2014), who performed model tests for a RoPax ship. A line drawing of the ship is shown in Fig. 7 and the main dimensions and weight data are presented in Table 7.

The numerical domain is presented in Fig. 8. It is expected that reflections and radiations from the ship hull towards the inlet boundary are relatively small in comparison to the box case; thus, the distance between the inlet boundary and the hull is reduced to two wave lengths, reducing the number of cells significantly. Deep sea conditions are modelled by applying a numerical domain that is one wave length deep. The effect of wave reflections from the side boundary is reduced by applying a domain that is two wave lengths wide. Only head sea conditions are studied and symmetric behaviour can be assumed, which allows modelling of only half of the vessel and the computational

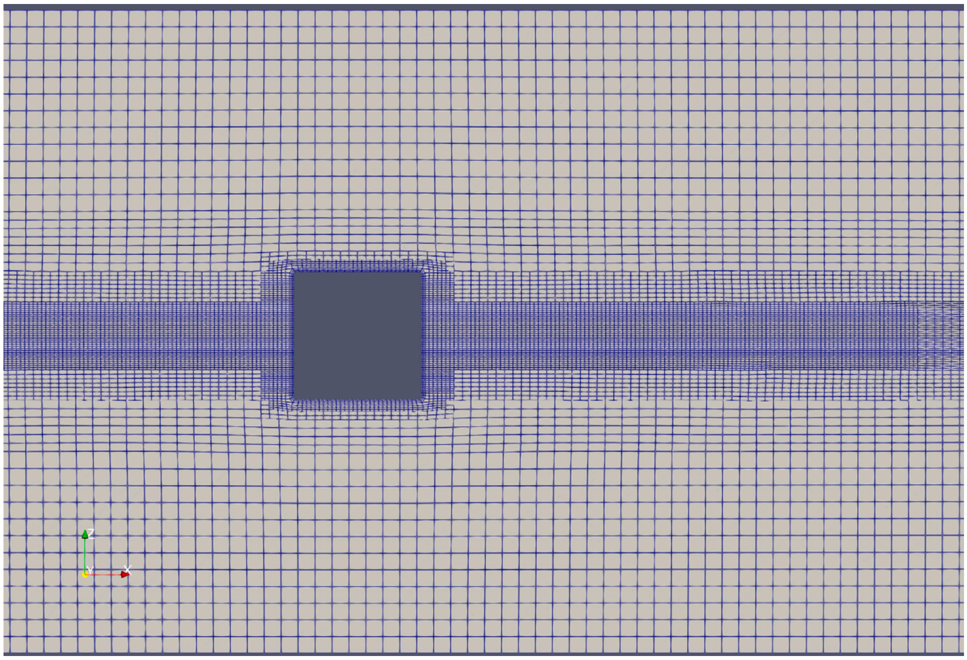

Fig. 6. An example of a computational mesh for the case $kb = 0.4$ ($H/\Delta z = 15$ and $AR = 2$).

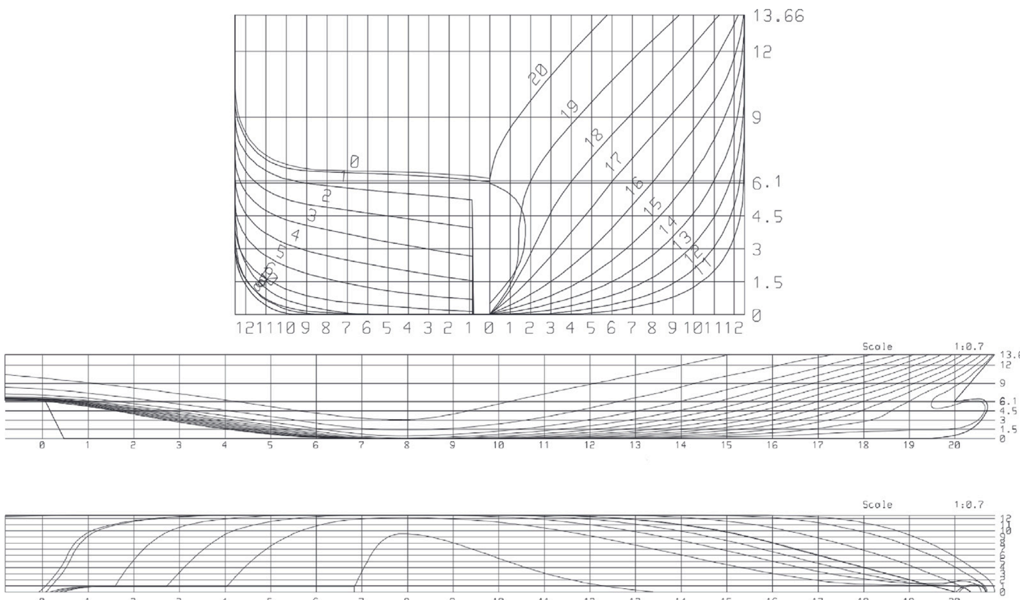

Fig. 7. Line drawing of the RoPax ship that was studied Kukkanen and Matusiak (2014).

domain. The same boundary conditions as with the box case are applied (see Tables 5) with the exception of the symmetry plane condition at the bottom and each side of the domain. The symmetry condition at the bottom and the side boundaries can be justified with the meshing methods that are applied. Coarsening the mesh before these boundaries aims to dampen the flow velocities in a non-tangential direction relative to these boundaries. Moreover, relaxation zones one wave length long are applied at the inlet and outlet ends of the computational domain.

The mesh that is applied is based on the box case results; thus the details of the mesh are introduced in Section 6.5. The same constant terms are applied as with the box case (see Table 6) but the sea water density is applied ($\rho_{water} = 1025$ kg/m^3). Three wave lengths and two wave heights are studied (see Table 8). Each case is modelled for about 22 wave periods to reach a steady state. Only heave and pitch motions are studied; therefore, all other motions are restricted

Table 7
Main dimensions and weight data of the RoPax ship that was studied Kukkanen and Matusiak (2014).

Quantity	value
Length between perpendiculars (L)	158 m
Breadth (B)	25 m
Draught (T)	6.1 m
Displacement (∇)	13766 m^3
Block coefficient (C_B)	0.55
Centre of gravity (x_{CG}, y_{CG}, z_{CG})	(74.9, 0.0, 10.9) m
Radius of gyration in pitch (k_{yy}/L)	0.25

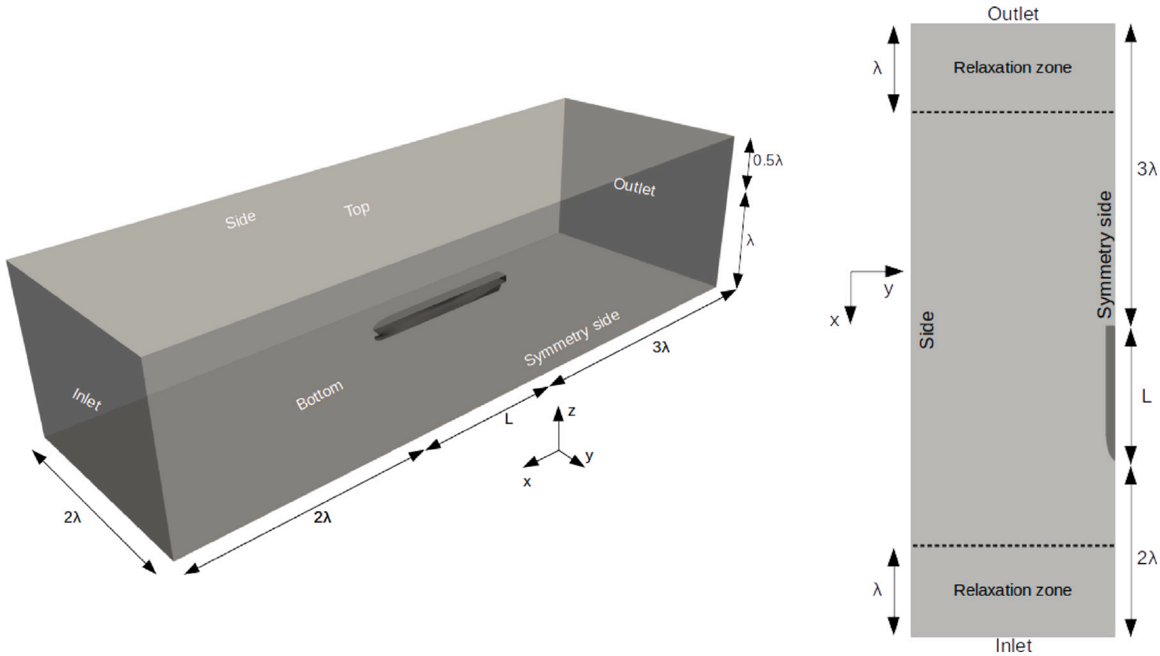

Fig. 8. Computational domain applied for the RoPax ship case.

Table 8
Wave study cases for the RoPax ship.

kL	k [1/m]	λ [m]	ω_w [1/s]	T [s]	ka ($H = 1.9$ m)	ka ($H = 4.1$ m)
4.0	0.025	248.2	0.50	12.6	0.02	0.05
4.8	0.031	205.1	0.54	11.5	0.03	0.06
7.8	0.050	126.6	0.70	9.0	0.05	0.10

during the simulation. The mesh deformation distances are set to be the expected motion amplitude of the bow and the stern of the ship for `innerDistance` considering heave and pitch coupling and a value that is ten times larger for `outerDistance`.

6. Numerical results

6.1. Accurate wave modelling

Figs. 9 and 10 show the effects of the mesh density on the modelled wave amplitude at wave probes P1-P3 for the case $kb = 0.2$ with steepnesses of $ka = 0.05$ and $ka = 0.1$ respectively while having a constant cell aspect ratio of $AR = 1$. For both steepness cases the mesh densities $H/\Delta z = 10$, 15, and 20 match well against each other, while $H/\Delta z = 5$ differs. After reaching a steady state, the $H/\Delta z = 20$ results show a slightly lower amplitude than the theoretical amplitudes for second-order waves (StokesII in OpenFOAM terminology). Coarser meshes predict higher wave amplitudes and $H/\Delta z = 5$ predicts clearly higher amplitudes than the theory. This effect is increased with lower wave heights ($ka = 0.05$). The increase in amplitudes is expected to be due to the artificial compression term in Eq. (16). Additionally, the results show that the wave amplitudes initially reach the theoretical values in all mesh cases when the wave group reaches the probe location. After some time the amplitudes reduce slightly with denser meshes, while $H/\Delta z = 5$ shows an increase in amplitudes at the probes P1 and P2, which are closer to the inlet boundary. The reason behind this is that some wave reflections occur from the relaxation zone at the outlet end of the domain. The effect of the reflection is larger in the denser meshes because of the more accurate wave modelling and the reflections with an $H/\Delta z = 5$ mesh cause an increase in amplitudes.

Similar trends are also visible with shorter wave cases ($kb = 1.2$ and $ka = 0.05$ and 0.1) (see Figs. 11 and 12). The wave amplitude measurements with densities $H/\Delta z = 10$, 15, and 20 are even closer to each other than with the longer wave length case for both steepnesses. $H/\Delta z = 5$ varies from the denser mesh results in a similar way to the $kb = 0.2$ cases. An exception to this is the probe P1 measurements for steepness $ka = 0.05$, where $H/\Delta z = 5$ matches higher densities. The effect of reflections is larger with the short wave length case than with the longer one. This is visible as a larger change in the measured wave amplitudes in time for both steepnesses and at all three probes.

When the amplitudes between the locations P1-P3 are compared, it can be seen that the predicted amplitudes increase further from the inlet boundary. The effect is stronger with coarser mesh cases and low wave amplitudes. At P1, $H/\Delta z = 5$ matches well with denser meshes and at P3 the difference in amplitudes is significant (see Fig. 11). The effect could be attributed to the artificial compression term in the MULES algorithm (see Eq. (16)). A similar increase in the wave amplitude resulting from the compression term was identified by Larsen et al. (2019).

The small differences in trends between the cases $kb = 0.2$ and $kb = 1.2$ can be explained by the depth of the NWT staying constant while the wave is scaled down to a smaller wave length. For $kb = 0.2$ the waves travel in a tank with an intermediate water depth, while $kb = 1.2$ corresponds to deep water waves. The differences can be expected to be due to the challenges of modelling between waves at deep or intermediate water depths.

Overall, a mesh density with $H/\Delta z = 10$ is accurate enough for regular wave modelling, especially in large 3D cases where the cell count becomes an issue. These results confirm previously published studies (Connell and Cashman, 2016; Roenby et al., 2017). The change in the modelled amplitude resulting from reflections from the outlet side relaxation zone increases with more dense meshes. In this paper, the total number of cells is relatively small; thus, a mesh density $H/\Delta z = 15$ is applied with the rest of the results that are presented.

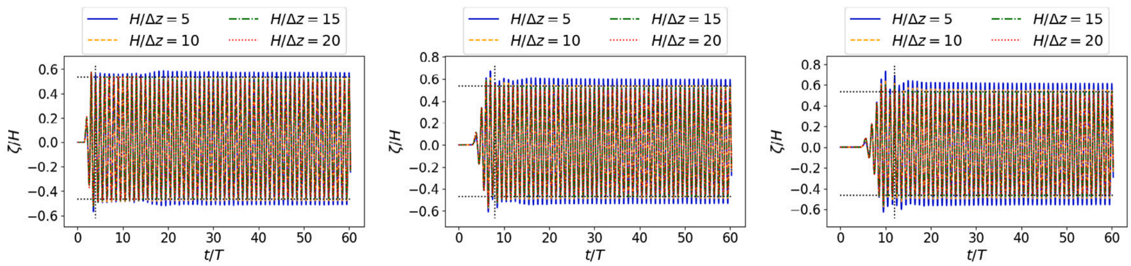

(a) P1 (b) P2 (c) P3

Fig. 9. The effect of mesh density on the wave amplitude at wave probes P1-P3 with the case kb = 0.2 and ka = 0.05. The dashed lines are the theoretical crest and through amplitudes for the StokesII wave and time instance when the wave group reaches the probe location.

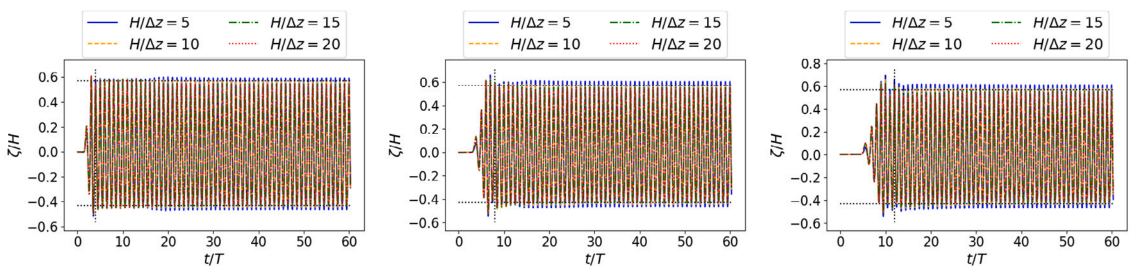

(a) P1 (b) P2 (c) P3

Fig. 10. The effect of mesh density on the wave amplitude at wave probes P1-P3 with the case kb = 0.2 and ka = 0.1. The dashed lines are the theoretical crest and through amplitudes for the StokesII wave and time instance when the wave group reaches the probe location.

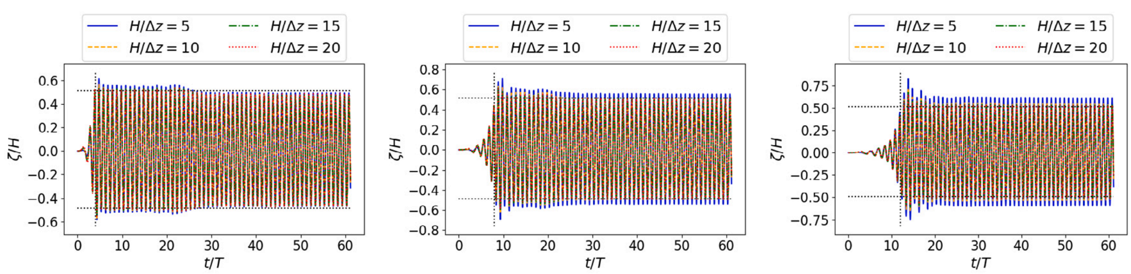

(a) P1 (b) P2 (c) P3

Fig. 11. The effect of mesh density on the wave amplitude at wave probes P1-P3 with the case kb = 1.2 and ka = 0.05. The dashed lines are the theoretical crest and through amplitudes for the StokesII wave and time instance when the wave group reaches the probe location.

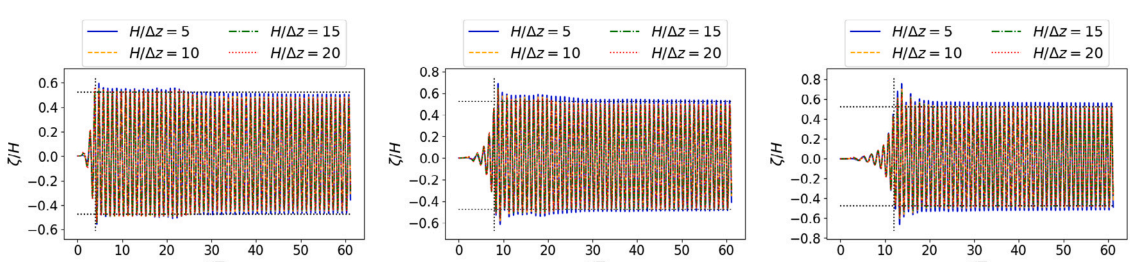

(a) P1 (b) P2 (c) P3

Fig. 12. The effect of mesh density on the wave amplitude at wave probes P1-P3 with the case kb = 1.2 and ka = 0.1. The dashed lines are the theoretical crest and through amplitudes for the StokesII wave and time instance when the wave group reaches the probe location.

The number of outer correctors (see `nOuterCorrectors` in Table 1, `nOCorr` from now on) specifies how many times fluid equations are iterated during one time step (see Fig. 1). Pure wave modelling results show that solving equations just once is enough; however, multiple iteration rounds may be essential for the accurate modelling of the excitation forces and motions of a floating body. Additionally, the `upwind` divergence scheme has a strong diffusive characteristic which may dampen the force and motion results too much. Turbulence modelling is required in many wave-structure interaction studies, such as wave breaking in bow slamming studies. The inclusion of turbulence

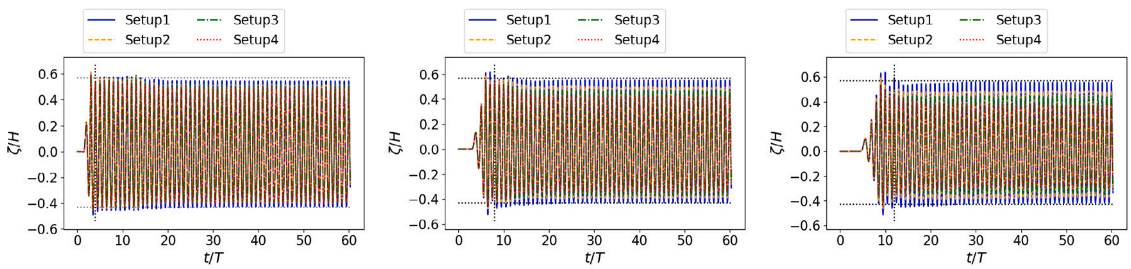

(a) P1 (b) P2 (c) P3

Fig. 13. The effect of the numerical setup on the wave amplitude at wave probes P1-P3 with the case $kb = 0.2$ and $ka = 0.1$. The dashed lines are the theoretical crest and through amplitudes for the StokesII wave and time instance when the wave group reaches the probe location.

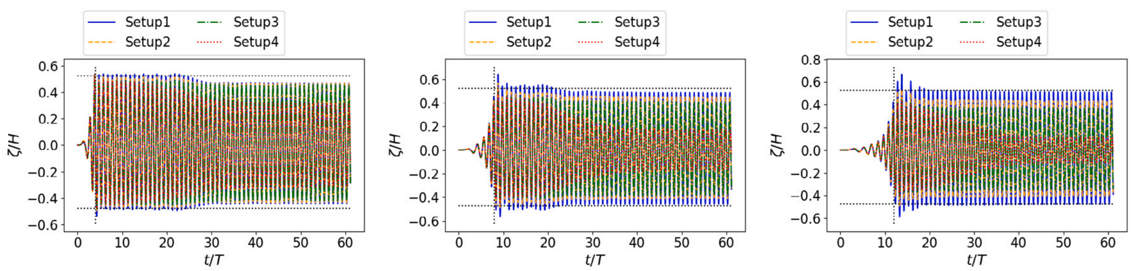

(a) P1 (b) P2 (c) P3

Fig. 14. The effect of the numerical setup on the wave amplitude at wave probes P1-P3 with the case $kb = 1.2$ and $ka = 0.1$. The dashed lines are the theoretical crest and through amplitudes for the StokesII wave and time instance when the wave group reaches the probe location.

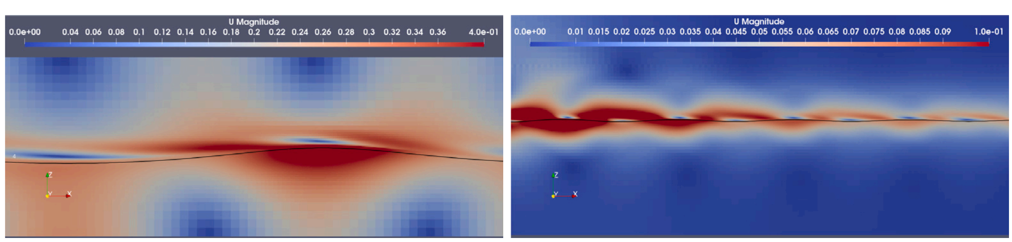

(a) $kb = 0.2$ (b) $kb = 1.2$

Fig. 15. Velocity magnitude profile with the cases $kb = 0.2$ and $kb = 1.2$. Profiles are between $\lambda - 2\lambda$ ($kb = 0.2$) and $\lambda - 5\lambda$ ($kb = 1.2$) from the inlet. The black curve shows the location of the free surface.

may influence wave modelling. Therefore, Figs. 13 and 14 show comparisons of `Setup1` - `Setup4` for the cases $kb = 0.2$ and 1.2 with a steepness $ka = 0.1$ (see Tables 1 and 2).

The results show that increasing the `nOCorr` value reduces the modelled amplitude. This effect is stronger in short waves. Increasing the `nOCorr` value more from value 8 applied in `Setup3` does not change the modelled amplitudes. This is due to numerical calculations converging during one time step. Similar reductions of wave amplitude due `nOCorr` value were observed by Larsen et al. (2019), Weber (2016). The authors speculate that the reason is computing the free surface location multiple times with the MULES algorithm during one time step. The less diffusive time and divergence schemes in `Setup2` - `Setup4` do not improve the wave modelling because of this. The strict requirements for mesh density and a small time step through a small maximum Courant number cause the higher numerical diffusion in the numerical schemes of `Setup1` not to matter.

The wave amplitude decreases in time with turbulence modelling, while all laminar setups reach a steady state quickly after the wave group has reached the probe location. The reduction of amplitude as a result of the turbulence modelling is increased further away from the inlet boundary and, especially, with shorter wave cases ($kb = 1.2$; see Fig. 14). The reason behind this is also expected to be to the MULES algorithm, which causes high velocities close to the free surface on the air phase side, as shown in Fig. 15. These high velocities with the application of turbulence modelling cause significant production of turbulence and thus very high levels of turbulent eddy viscosity. An example of this is shown in Fig. 16, where the turbulence viscosity has a value more than 1,000 times larger than the physical kinematic viscosity $\nu = 1.0 \times 10^{-6} \frac{m^2}{s}$. This artificially increases the total viscosity close to the free surface, which dampens the wave amplitude. The dampening is stronger in short waves as a result of the high velocities related to the wave propagation that may occur only close to the free surface (see Fig. 15). In this study, the modelled waves are physically small. Therefore, it is expected that in seakeeping cases with full-scale or even model-scale analysis the damping effect resulting from turbulence modelling will not be as significant.

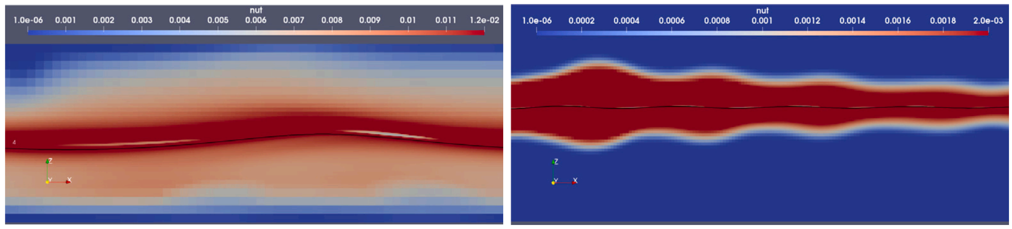

(a) $kb = 0.2$ (b) $kb = 1.2$

Fig. 16. Turbulent kinematic viscosity (nut) profiles for the cases $kb = 0.2$ and $kb = 1.2$. The profiles are between $\lambda - 2\lambda$ ($kb = 0.2$) and $\lambda - 5\lambda$ ($kb = 1.2$) from the inlet. The black curve shows the location of the free surface.

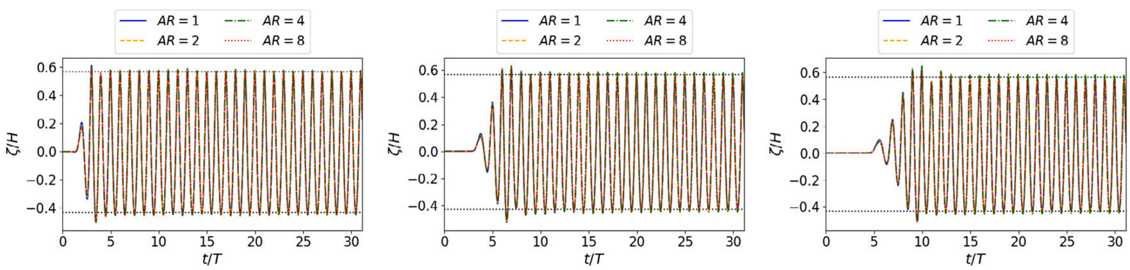

(a) P1 (b) P2 (c) P3

Fig. 17. The effect of the mesh aspect ratio on the wave amplitude at wave probes P1-P3 with the case kb = 0.2 and ka = 0.1. The dashed lines are the theoretical crest and through amplitudes for the StokesII wave.

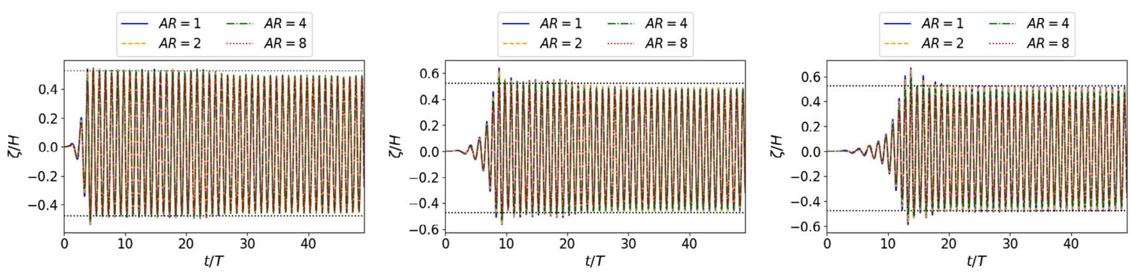

(a) P1 (b) P2 (c) P3

Fig. 18. The effect of the mesh aspect ratio on the wave amplitude at wave probes P1-P3 with the case kb = 1.2 and ka = 0.1. The dashed lines are the theoretical crest and through amplitudes for the StokesII wave.

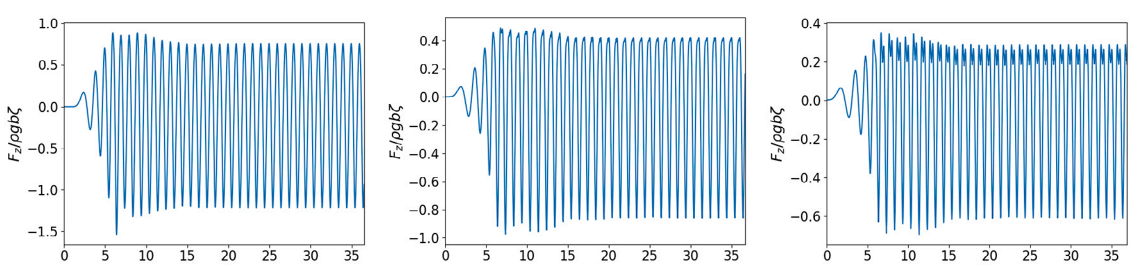

(a) $kb = 0.4$ (b) $kb = 0.7$ (c) $kb = 1.0$

Fig. 19. Time histories of modelled heave excitation forces for the cases $kb = 0.4, 0.7$, and 1.0 with $ka = 0.1$.

Figs. 17 and 18 show the effect of the cell aspect ratio on the modelled wave amplitude. Closer to the inlet boundary, the large aspect ratio increases the modelled wave amplitude marginally in comparison to $AR = 1$ (P1 and P2 for $kb = 0.2$ and P1 for $kb = 1.2$). Far away from the inlet, the larger aspect ratio reduces the modelled amplitudes. This effect increases with larger aspect ratios. Previous studies also showed that a larger aspect ratio affects the waves because of the increase in the horizontal flux of α inside the cell. This increases the wave amplitude close to the wave source. Consequently, increased wave steepness can cause earlier wave breaking, which in turn reduces the wave amplitude far away from the source (Roenby et al., 2017; Jacobsen et al., 2012b). The effect of the change in the measured amplitude is stronger with $kb = 1.2$, which is expected to relate to the modelling of waves in deep waters or at intermediate depths. In general, the aspect ratio $AR = 2$

Table 9
Incident amplitudes by the method of Goda and Suzuki (1976).

Case	ζ (Setup1)	ζ (Setup2)
$kb = 0.4$	0.058	0.059
$kb = 0.7$	0.034	0.033
$kb = 1.0$	0.024	0.022

Table 10
The average time step with each motion solver and total wall-clock time.

	$T/\Delta t_{avg}$	Wall-clock time [s]
Newmark	2955	19 223
Crank–Nicolson	2955	16 698
symplectic	2957	16 839

Table 11
Comparison of RAOs with different D_a and experiments when $kb = 0.5$ and $ka = 0.1$.

Setup	RAO
$D_a = 0.4$	0.41
$D_a = 0.6$	0.99
$D_a = 0.99$	1.23
experiments	1.39

matches well against $AR = 1$ throughout the domain and $AR = 4$ leads to similar results in the way of the inlet (P1 and P2 locations). $AR = 8$ is too large unless the floating body is modelled very close to the inlet boundary; however, the modelled structure is usually located a few wave lengths away from the inlet boundary (between the locations P1 and P2). Thus, a maximum aspect ratio of $AR = 4$ is recommended as the most efficient ratio in cases with large numbers of cells. For the rest of the cases in this paper the total number of cells is small. Therefore, $AR = 2$ is applied.

In conclusion, accurate and stable waves can be propagated with the distance of multiple wavelengths with the numerical setup presented by Larsen et al. (`Setup1`) (Larsen et al., 2019) and using the recommended mesh density of at least 10 cells per wave height (Roenby et al., 2017). The setup is also most efficient among the ones compared as the smallest number of calculations is performed during one time step as a result of the lowest `nOCorr` value. Efficiency can also be increased by applying an aspect ratio up to $AR = 4$ instead of the $AR = 1$ that was recommended by previous studies (Roenby et al., 2017; Jacobsen et al., 2012b). The artificial free surface compression term in the MULES algorithm can cause some unexpected behaviour, as was seen with larger wave amplitudes with a mesh density of $H/\Delta z = 5$ and a reduction of wave amplitude when the `nOCorr` value was increased. Turbulence modelling can artificially increase fluid viscosity close to the free surface, which reduces the wave amplitude, at least for physically small waves as in this study.

6.2. Excitation force modelling

The wave modelling results showed that $H/\Delta z = 15$ and $AR = 2$ are accurate for propagating waves from the inlet; thus, these are applied for modelling the excitation forces. Fig. 19 shows the time histories for the heave excitation force for the cases $kb = 0.4, 0.7$, and 1.0 with $ka = 0.1$. The input amplitude based on Table 4 is applied to make the results non-dimensional. It is seen that in all cases the force amplitudes diminish slightly after reaching the initial peak values at around $t/T = 6$ when the wave group reaches the box and this effect is increased in longer waves. At around $t/T = 15$ a steady state is reached. The reduction in peak amplitudes is due to some of the reflections from the box towards the inlet getting re-reflected in the inlet relaxation zone.

For each case, the last few modelled steady state periods are compared against the experimental excitation forces measured by Rodríguez and Spinneken (2016) as shown in Fig. 20. In general a good match is achieved; however, the modelled negative peaks are slightly overestimated in comparison to the experiments. The nonlinear positive peak forces in the cases $kb = 0.7$ and 1.0 show a good match between the modelled results and the experiments. The results show that the best numerical setup for wave modelling (see Table 1) is also accurate and able to reveal the nonlinear nature of wave excitation forces.

Similarly to pure wave modelling, the effect of the chosen numerical setup is studied (see `Setup1` and `Setup2` in Tables 1 and 2). The wave amplitude diminishes with `Setup2` (see Figs. 13 and 14), which also affects the excitation force results. Therefore, to apply the actual modelled wave amplitude reaching the box in the non-dimensionalised force results, the measured wave amplitudes at the wave probes P1 and P2 are decomposed into incoming and reflected wave amplitudes according to the method presented by Goda and Suzuki (1976). The incident amplitudes are shown in Table 9 and these values are applied in non-dimensionalising the excitation force results in Fig. 21. The amplitudes follow the previously presented trend; however, for $kb = 0.4$, `Setup2` has a higher amplitude than `Setup1`. This could be due to the combination of $AR = 2$ and the numerical schemes that were applied with `nOCorr` $= 2$, causing the amplitude to increase. The inaccuracy of the decomposition method could also be the reason.

The force results (Fig. 21) show that for the case $kb = 0.4$ the modelled force is also slightly reduced with `Setup2`, while this setup does not have an effect on the force amplitudes in the cases $kb = 0.7$ and 1.0. The latter is related to the reduction of the wave amplitude with `Setup2`, which is stronger in longer waves. Additionally, the inaccuracy of the decomposition method resulted in the higher incident wave amplitude which is applied when making the results non-dimensional. The two short wave length cases ($kb = 0.7$ and 0.1) show noise in the force results, which is increased with shorter wave lengths. The reason for the numerical noise is expected to be due to the numerical setup. In `Setup1`, the divergence scheme that is applied is the upwind scheme, which has a very diffusive property. However, the `limitedLinearV` scheme in `Setup2` is less diffusive. Additionally, increasing the blending factor from 0.3 to 0.625 in the `CrankNicolson` time scheme changes the scheme closer to a pure Crank–Nicolson form, which is less diffusive than the implicit Euler scheme (OpenFOAM, 2023). In conclusion, `Setup1` includes enough numerical diffusion, which dampens the possible instabilities so that numerical noise does not occur, while `Setup2` has reduced stability for noise to occur.

6.3. Accurate motion modelling

In this subsection, the numerical setup presented in Table 1 is verified for motion modelling. The motion modelling setups (see Fig. 2) are studied for the resonance frequency at $kb = 0.5$, which corresponds to the largest expected motions and steepness, $ka = 0.1$ (Rodríguez and Spinneken, 2016). The three numerical solvers (Newmark, Crank–Nicolson, and symplectic) have been compared while keeping the acceleration relaxation term $R_a = 0.6$ and the damping term $D_a = 0.99$. An exception to this was the setting $R_a = 0.3$ when applying the symplectic solver because of the simulation crashing after a while with $R_a = 0.6$ as a result of the velocity of the box approaching infinity. The results are shown in Fig. 22 and show that the solver has no effect on motions. This could be attributed to the very small time steps throughout the simulations (see Table 10). The small time steps are due to the small defined maximum Courant number ($Co_{max} = 0.3$) which is required for accurate wave modelling. Notwithstanding this, applying the Crank–Nicolson and symplectic solvers is significantly faster than applying the Newmark solver.

The effect of the R_a and D_a factors on the heave motion was studied while using the Newmark solver. The results shown in Fig. 23 show that varying R_a does not have an effect on the motion amplitudes.

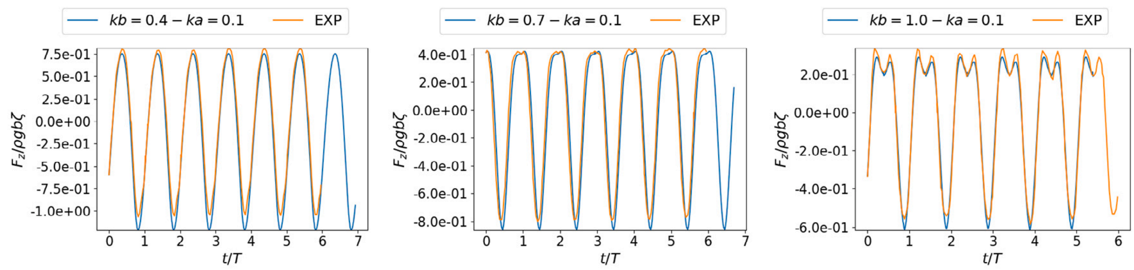

(a) $kb = 0.4$ (b) $kb = 0.7$ (c) $kb = 1.0$

Fig. 20. Comparison of the heave excitation force between the modelling results and experiments for the cases $kb = 0.4, 0.7$ and 1.0 with $ka = 0.1$. The input amplitude for the wave is used to make the forces non-dimensional.

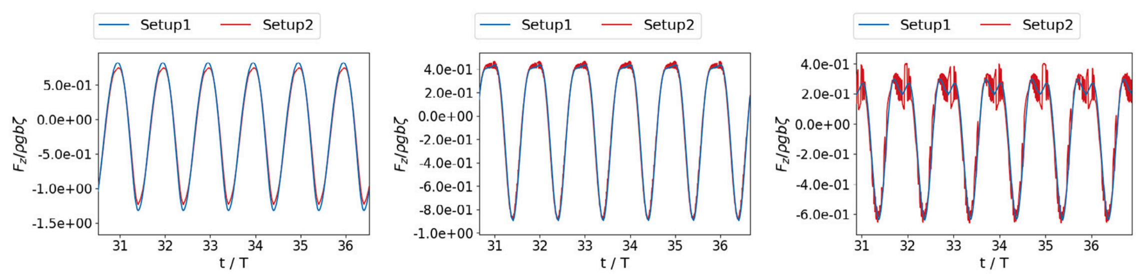

(a) $kb = 0.4$ (b) $kb = 0.7$ (c) $kb = 1.0$

Fig. 21. Comparison of the numerical setup for the modelling of the heave excitation force with the cases $kb = 0.4, 0.7$, and 1.0 and $ka = 0.1$. The incident amplitude (see Table 9) for the wave is used to make the forces non-dimensional.

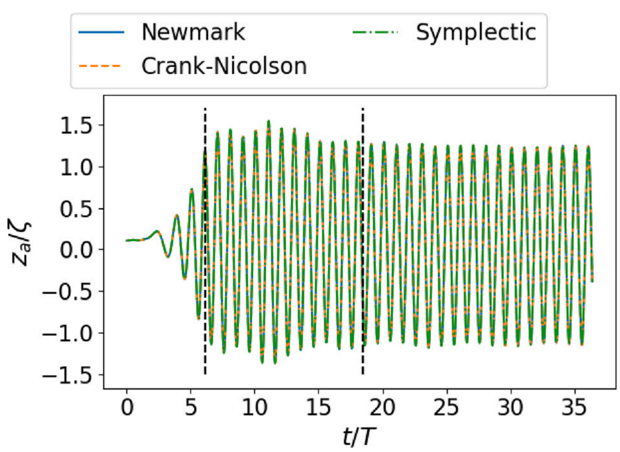

Fig. 22. The effect of the motion solver on the motion results. The black lines show the time instances when the wave group (earlier) and possibly re-reflected waves from the inlet (later) reach the box.

This is expected also to be due to the very small time steps used during the simulations. On the other hand, D_a has a clear effect on the motion amplitudes. A lower value for D_a reduces the computed value for velocity at each time step, which directly affects the amplitudes of motions (see Fig. 2). RAOs can be calculated from the motion results by taking half of the average of the positive and negative peak distances. Table 11 shows the comparison of the RAO values between the three D_a values and experimental measurements (Rodríguez and Spinneken, 2016). It is seen that $D_a = 0.99$ is closest to the experimental value but slightly underestimates motions. The results show that small D_a values cannot be applied and no damping in the velocity calculation ($D_a = 0.99$) is recommended.

In conclusion, the motion solver and R_a factor do not have any effect on motions because of the small simulation time steps required for accurate wave modelling. However, the solver can influence computational efficiency. It is noted that R_a also affects the stability of the simulation. For example, reducing the value of R_a can make the simulation more stable and prevent it from crashing, as was seen with the symplectic solver. On the basis of current results, the Crank–Nicolson solver is recommended because of its computational efficiency over the Newmark solver and its numerical stability over the symplectic solver by allowing a larger R_a value without the simulation crashing. On the other hand, D_a has a large effect on the motion amplitudes and should be kept high to get the most accurate results in comparison to the experiments.

Table 12
$T/\Delta t_{avg}$ for each wave case with the two numerical setups.

Case	Setup1		Setup2	
	$ka = 0.05$	$ka = 0.1$	$ka = 0.05$	$ka = 0.1$
$kb = 0.2$	6994	3566	8854	5566
$kb = 0.4$	3799	3138	33 851	9523
$kb = 0.5$	3855	2955	17 146	10 030
$kb = 0.7$	4937	3747	33 052	16 019
$kb = 1.0$	5704	4238	32 004	22 365
$kb = 1.2$	1866	1612	3934	3486

6.4. Response amplitude operators

The RAOs are computed for all the wave cases presented in Table 4. The Crank–Nicolson motion solver, $R_a = 0.6$, and $D_a = 0.99$ are applied as they proved to be computationally efficient and stable. The results are shown in Fig. 24, which also presents error bars computed with the standard deviation of the RAO values. The excitation force and motion modelling results suggest that some wave reflections and radiated waves from the box towards the inlet boundary get re-reflected, which reduces the force and motion amplitudes (see Figs. 19, 22, and 23). This is considered in the RAO calculations (see Fig. 24) by applying two different time spans. RAOs with re-reflections are

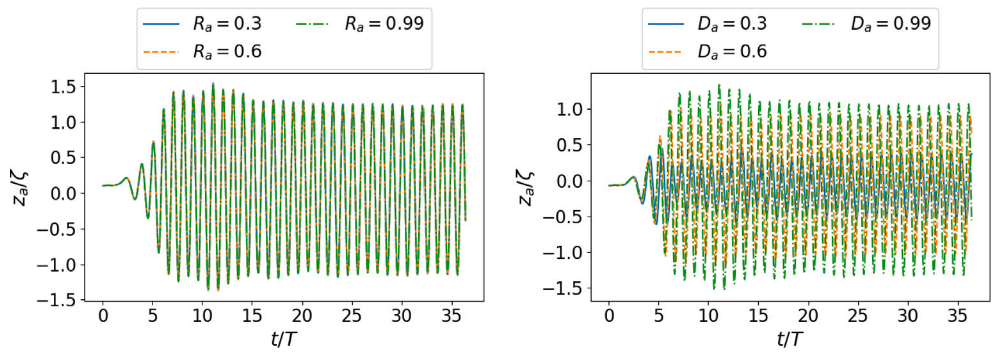

Fig. 23. The effect of R_a and D_a, respectively, on the motion results.

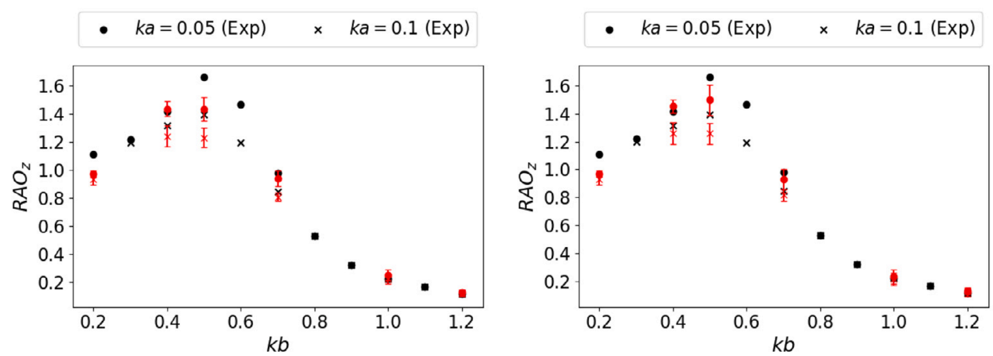

(a) With re-reflections

(b) Without re-reflections

Fig. 24. Comparison of modelled RAOs against experimental measurements with the inclusion of re-reflections and not including them.

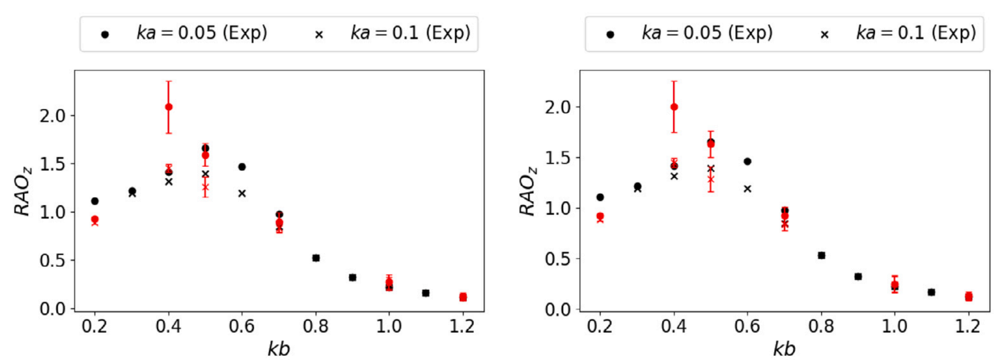

(a) With re-reflections

(b) Without re-reflections

Fig. 25. Comparison of modelled RAOs with `Setup2` against experimental measurements with the inclusion of re-reflections and not including them.

computed by considering the time range starting from when the wave group reaches the box until the end of the simulation. On the other hand, RAOs without re-reflections only include the time range until the re-reflected waves reach the box (see Fig. 22). It is seen that the computed RAOs match well against the experimental measurements. The nonlinear effect of steeper waves reduces the motion amplitudes for large-amplitude motions and may be visible in the numerical results (kb = 0.4, 0.5, and 0.7). However, close to the resonance frequency ($kb = 0.5$) the computed RAOs underestimate the experimental RAOs. The error is also largest close to the resonance frequency, which is due to the largest changes in motion amplitude as a result of reflected and radiated waves. The influence of the large change in the wave amplitude is also visible in Fig. 22. Not including the re-reflections increases the RAO values because of the inclusion of a shorter time span into the RAO calculation and not considering the reduced motion amplitude. However, this also increases the uncertainty as the changes in the motion amplitude are large inside this time range as a result of the initial transient behaviour of motion.

Similarly to the excitation force cases, the effect of the numerical setup is studied by also applying `Setup2` for the RAO calculations (see Fig. 25). This setup seems to improve the numerical prediction of RAOs against the experiments close to the resonance frequency. However, the increased instability of the numerical setup may lead to unexpected behaviour. For example, see $kb = 0.4$ with steepness $ka = 0.05$, which shows a very large RAO value and uncertainty for the RAO. It is noted that the $kb = 0.4$ case did not show any significant instabilities in

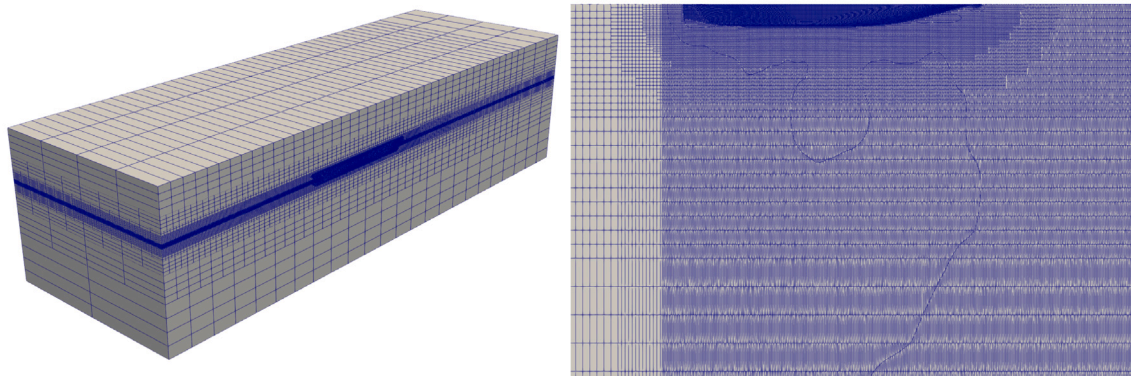

(a) Overall view of the mesh (b) Mesh at the still water level close to the ship hull

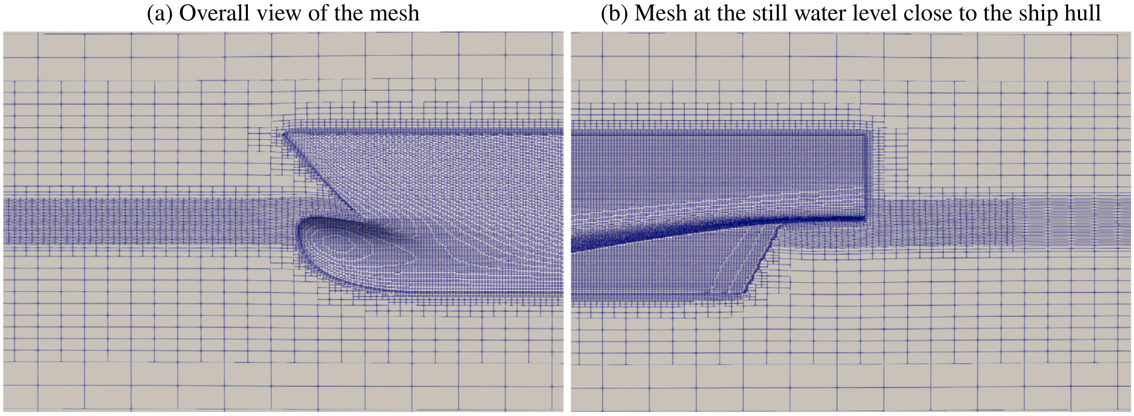

(c) Mesh around the bow (d) Mesh around the stern

Fig. 26. Mesh applied for the RoPax ship cases. An example from the case $kL = 7.8$ and $ka = 0.05$.

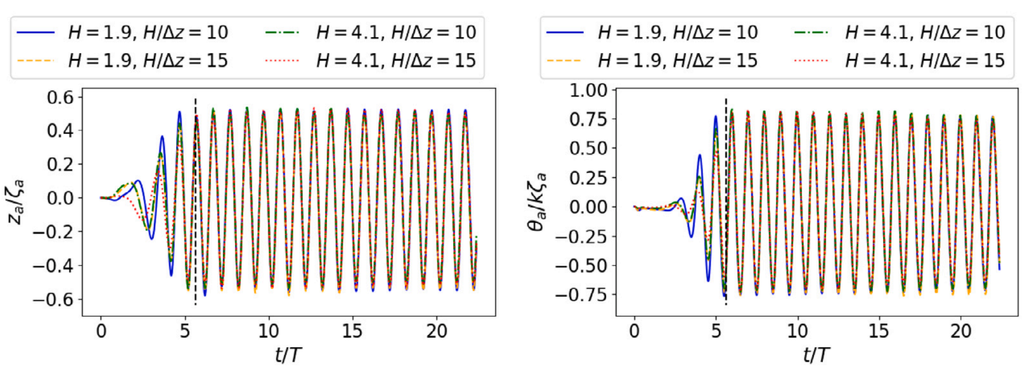

(a) Heave (b) Pitch

Fig. 27. Heave and pitch motion time histories for the case $kL = 4.0$. The black line shows when the wave group reaches the aft part of the hull.

the excitation force modelling (see Fig. 21). Therefore, it is assumed that the inclusion of motions in `Setup2` increases instabilities. Because of the numerical instability the time step is greatly reduced, thus increasing the computational time (see Table 12). As the time step is controlled by the maximum Courant number, it is assumed that the instabilities cause large local velocities close to the box, which reduces the time step (see Eq. (15)).

6.5. 3D RoPax ship case

On the basis of the box case results, `Setup1` is applied for the 3D case with the RoPax ship for three wave lengths and two wave heights. However, the $k-\omega$ SST turbulence model is applied as the simulation is performed for a full-scale ship. The `CrankNicolson` solver and values $R_a = 0.5$ and $D_a = 0.99$ are applied for the dynamic mesh settings. Mesh densities of $H/\Delta z = 10$ and 15 are applied to study the effect of mesh density in the 3D domain too (see Fig. 26). Similarly to the box case, the densest mesh area for accurate wave modelling is two wave heights high in the vertical direction around the still water level. A mesh aspect ratio of $AR_{xz} = 4$ is applied in the direction of wave propagation. It is assumed that the mesh aspect ratio can be larger in the direction perpendicular to the wave propagation far away from the ship hull; thus, in front of and behind the ship the mesh aspect ratio $AR_{xy} = 4$ is applied for the wave height $H = 4.1$ m and $AR_{xy} = 8$ for the wave height $H = 1.9$ m to reduce the number of cells. Further mesh coarsening close to the empty side boundary is applied to reduce the number of cells and to dampen reflected or radiated waves from the ship towards the side boundary. Close to the ship hull the mesh is

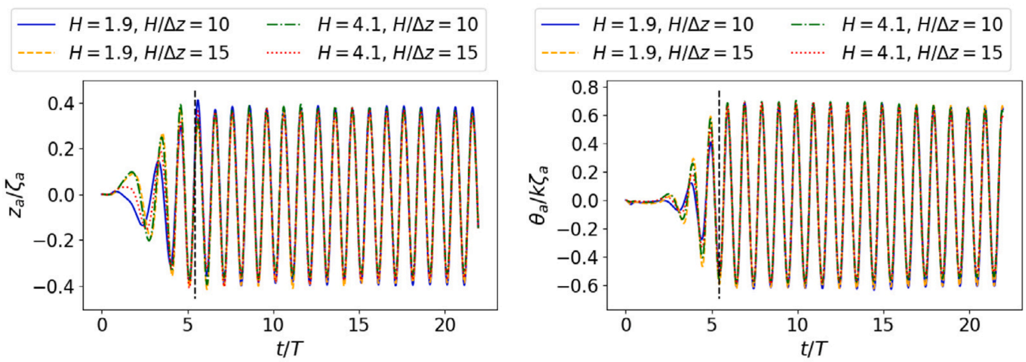

(a) Heave (b) Pitch

Fig. 28. Heave and pitch motion time histories for the case $kL = 4.8$. The black line shows when the wave group reaches the aft part of the hull.

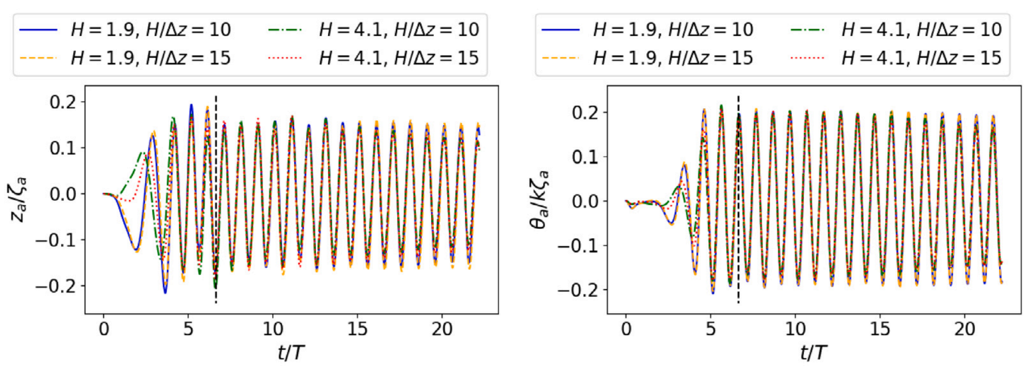

(a) Heave (b) Pitch

Fig. 29. Heave and pitch motion time histories for the case $kL = 7.8$. The black line shows when the wave group reaches the aft part of the hull.

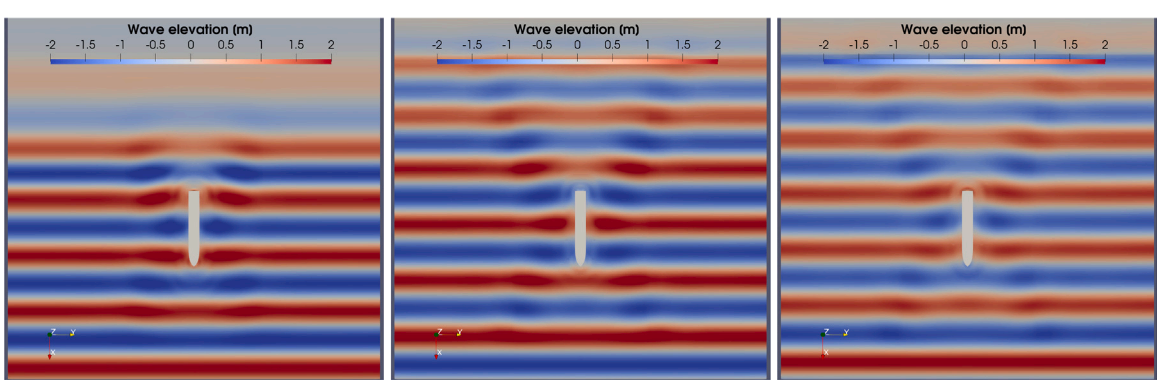

(a) $t = 8.9T$ (b) $t = 14.4T$ (c) $t = 20.0T$

Fig. 30. Wave field at three time instances ($t = 8.9T$, $14.4T$ and $20.0T$) for the case $kL = 7.8$, $H = 4.1$ and $H/\Delta z = 10$. Modelled wave amplitude is reduced due to wave reflections on the outlet side mesh coarsening steps.

refined so that in the horizontal plane the mesh aspect ratio becomes one, $AR_{xy} = 1$. Moreover, further refinements are applied in all three coordinate directions to model the ship hull accurately. Towards the outlet boundary the mesh is coarsened in the flow direction to reduce the number of cells and to dampen the waves.

Figs. 27–29 show the heave and pitch time histories for the three wave length cases. The figures show that stable heave and pitch motions are achieved with both mesh densities. Additionally, the motion amplitudes are similar with both densities. Gradual reductions of peak amplitudes in time are visible, which is highlighted with shorter waves

Table 13
RAO values and standard distribution values for the RoPax ship case against experimental values (Kukkanen and Matusiak, 2014).

Case	Heave		Pitch	
	$H/\Delta z = 10$	$H/\Delta z = 15$	$H/\Delta z = 10$	$H/\Delta z = 15$
$kL = 4.0,\ H = 1.9$ m	0.53 ± 0.01	0.52 ± 0.01	0.76 ± 0.01	0.76 ± 0.01
$kL = 4.0,\ H = 4.1$ m	0.51 ± 0.01	0.52 ± 0.01	0.76 ± 0.01	0.73 ± 0.03
Experiments	0.58		0.80	
$kL = 4.8,\ H = 1.9$ m	0.38 ± 0.01	0.37 ± 0.01	0.64 ± 0.01	0.64 ± 0.01
$kL = 4.8,\ H = 4.1$ m	0.37 ± 0.01	0.37 ± 0.01	0.62 ± 0.01	0.61 ± 0.03
Experiments	0.38		0.62	
$kL = 7.8,\ H = 1.9$ m	0.16 ± 0.01	0.16 ± 0.01	0.19 ± 0.00	0.19 ± 0.00
$kL = 7.8,\ H = 4.1$ m	0.14 ± 0.01	0.14 ± 0.01	0.18 ± 0.01	0.17 ± 0.01
Experiments	0.12		0.16	

and larger wave heights (see Fig. 29). This is due to wave reflections occurring on the outlet side of the ship because of too-rapid mesh coarsening steps. These reflected waves combine with the incoming waves from the inlet and the total wave amplitude is smaller than the incoming waves (see Fig. 30). The model-scale wave modelling results showed dampening of the wave amplitude as a result of the turbulence modelling (see Figs. 13–16). Similar dampening is not visible in the RoPax vessel motion results; thus, the $k-\omega$ SST turbulence model is seen to be suitable for full-scale wave modelling problems.

Table 13 shows the RAO values and standard deviation for heave and pitch for each case and comparison to the experiments presented by Kukkanen and Matusiak (2014). The RAOs for the modelled values are computed from the time that the wave group reaches the aft part of the hull (see Figs. 27–29) until the end of the simulation. It can be seen that the modelled values are close to the experimental ones. The reduction of the peak amplitudes in time is visible as lower RAO values for higher wave height results with shorter wave cases (kL = 4.8 and 7.8) and also as larger standard deviation values, especially in pitch.

The modelled RAOs for the shortest wave length case ($kL = 7.8$) are overestimated in comparison to the experiments; however, small motions increase the relative inaccuracies in both the numerical modelling and experimental studies. On the other hand, the longest wave length case ($kL = 4.0$) shows underestimation of the RAOs in comparison to the experiments. One reason for the underestimation is the very large motions. Fig. 31 shows the mesh deformation and location of the free surface at time instances when the bow is diving deep underwater and rising high out of the water. It can be seen that the free surface is very close to the edge of the densest mesh area, which can disturb the flow close to the free surface, thus causing damping of the wave close to the hull. This can be avoided by increasing the dense mesh area but this increases the number of cells. Another option is to apply the overset method for the mesh motions, as it is suitable for large motions.

7. Discussion and conclusions

The pure wave modelling results agree with previously published research suggesting that the mesh density should be at least 10 cells per wave height for accurate wave modelling (Connell and Cashman, 2016; Roenby et al., 2017). Increasing $H/\Delta z$ to a value of over 10 does not increase the accuracy greatly; thus, $H/\Delta z = 10$ can be considered to be the most efficient mesh density. Additionally, the setup recommended by Larsen et al. (2019) (`Setup1`) shows good performance in keeping a constant wave height in time and throughout the numerical wave tank. Increasing the iterations of all the fluid equations during one time step (`nOuterCorrectors`) reduces the wave amplitude. This is because the free surface location is computed multiple times during one time step with the MULES algorithm. In 2D cases the physical size of the waves is small. Therefore, the inclusion of $k-\omega$ SST turbulence modelling reduces the wave amplitude in time as a result of artificially increasing the fluid viscosity close to the free surface. This is caused by spurious velocities in the air phase close to the free surface introduced numerically by the MULES algorithm. It is shown with the 3D ship study that in larger-scale waves the damping effect of the turbulence does not occur. Finally, the mesh aspect ratio can be increased up to $AR = 4$ before it has a significant effect on the wave amplitude while increasing the efficiency of the simulation by reducing the number of cells.

The optimal setup for wave modelling is also confirmed to be accurate in nonlinear heave excitation force modelling for a static box. The modelled forces matched the experimental values well. A comparison of `Setup1` and `Setup2` shows that a different numerical setup does not affect the modelled force amplitudes greatly. However, the time derivative and convection divergence schemes applied in `Setup2` reduce the stability of the simulation, causing numerical noise in force time histories. The noise becomes worse with shorter wave lengths. Therefore, it is concluded that `Setup1` offers enough numerical damping to reduce the numerical noise but does not reduce the accuracy of the excitation force modelling.

The study for accurate motion modelling shows that the motion solver and acceleration relaxation factor that is applied (R_a) does not affect the motion amplitudes as a result of the small time-step required for accurate wave modelling. However, the solver can have an effect on the required simulation times, as was seen with the Crank–Nicolson and symplectic solvers being faster than the Newmark solver. Additionally, R_a has an effect on the stability of the simulation. For example, reducing its value can increase stability, as was seen with the sympletic solver. In consequence, the Crank–Nicolson solver is recommended over the Newmark and symplectic solvers. Notwithstanding these, the acceleration damping factor (D_a) has a significant effect on the motion amplitudes. Comparison with the experimental results showed that neglecting damping ($D_a = 0.99$) during simulation results in the motion predictions closest to the experiments.

The RAO results show that the optimal numerical setup can model motions which match the experimental data well. The nonlinear effects related to the wave steepness are modelled accurately. However, larger differences from the experiments occur close to the resonance frequency, where the modelled RAOs show lower values and large uncertainty. The underestimated RAO and large uncertainty are expected to be due to re-reflections from the inlet side relaxation zone, which affect motion amplitudes. Applying `Setup2` improves the modelled RAOs close to the resonance frequency, but uncertainties increase as a result of the increased numerical instability. Because of this the simulation times are also significantly longer. Although `Setup1` includes strong numerical diffusion as a result of its time and divergence schemes it is a recommended setup in preference to `Setup2`. It is expected that because of the strict requirements for mesh density and time step, which are due to the need for a large number of cells per wave height and a small cell aspect ratio and small Courant number, additional diffusion does not reduce the accuracy of the modelling. On the contrary, `Setup1` introduces a suitable amount of diffusion to reduce the numerical noise from the result.

The application of `Setup1` and mesh densities of $H/\Delta z = 10$ and 15 with an aspect ratio $AR_{xz} = 4$ in the 3D case of a RoPax vessel shows that an accurate setup in 2D is also accurate in 3D simulation. The two mesh densities result in matching motion time histories and RAO values. Additionally, the RAOs match well against the experimental values. Slight underestimation is visible in very large motion, hinting that the overset method should be applied in preference to the deforming mesh method in large motions.

The results showed that a numerical setup for pure wave modelling offers accurate enough resolution for wave-structure interaction. However, this accuracy introduces re-reflections from the inlet relaxation zone, which affects the results by lowering the excitation forces and motion amplitudes. Reflections from the relaxation zone also had a small effect in the pure wave modelling results, where they altered

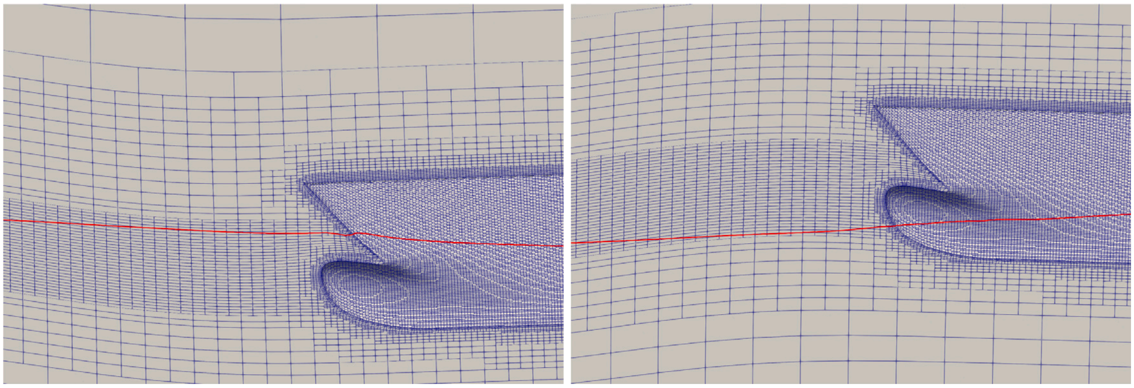

(a) Bow sinking deep underwater (b) Bow rising high from the water

Fig. 31. Visualisation of the mesh at the time instances when the bow is sinking underwater or rising high from the water. The red line shows the location of the free surface at the time instance.

the modelled wave amplitude. In the case of the modelling of motions, the effect of re-reflections is especially strong close to the resonance frequency, which was seen as large uncertainties. Additionally, the 3D RoPax ship case also showed the effect of reflections from the mesh coarsening steps. The reduction of these reflections should improve the modelled waves, forces, and motions, thus reducing the error in the RAOs, and improve the results in comparison to the experiments. Reflections inside the relaxation zones could possibly be reduced by changing the relaxation zone settings (Jacobsen et al., 2012a). Reflections resulting from the mesh coarsening steps can be reduced by increasing the number of cells between each coarsening step.

In conclusion, OpenFOAM with the waves2Foam toolbox can predict forces and motions with acceptable accuracy. The current study applied a 2D case with a simple box structure as a static structure or only with heave motion to find the optimal numerical setup for simulation, aiming for reduced computational cost and considered the experimental data as validation. The optimal setup was then applied in a more realistic study case for seakeeping by applying the setup to a 3D RoPax ship case in head waves while considering heave and pitch coupling. Accordingly, it is appropriate to study the effect of different mesh and numerical setups in wave-structure interaction modelling in simple 2D cases and then apply the results in more complex cases. Future research will expand these results in the full 6 DOF motion studies and oblique waves.

CRediT authorship contribution statement

Aaro Karola: Writing – review & editing, Writing – original draft. **Sasan Tavakoli:** Writing – review & editing, Writing – original draft. **Tommi Mikkola:** Writing – review & editing, Writing – original draft. **Jerzy Matusiak:** Writing – review & editing, Writing – original draft. **Spyros Hirdaris:** Writing – review & editing, Writing – original draft.

Declaration of competing interest

The authors declare that they have no known competing financial interests or personal relationships that could have appeared to influence the work reported in this paper.

Data availability

Data will be made available on request.

Acknowledgements

The authors wish to acknowledge CSC – IT Center for Science, Finland, for computational resources. The financial support from the Business Finland Co-Innovation project CaNeLis is greatly appreciated.

References

Acharya, A., De Chowdhury, S., Paloth, F.P., Datta, R., 2023. Numerical investigation of bottom slamming using one and two way coupled methods of S175 hull. Appl. Ocean Res. 139, 103684.
Afshar, M.A., 2010. Numerical Wave Generation in OpenFOAM R (Master's thesis). Chalmers University of Technology.
Akimoto, H., 1997. Finite-volume simulation of the flow around a sailing boat with unsteady motion. J. Soc. Nav. Archit. Japan 1997 (181), 35–44.
Armenio, V., 1998. Dynamic loads on submerged bodies in a viscous numerical wave tank at small KC numbers. Ocean Eng. 25 (10), 881–905.
Bekhit, A., Lungu, A., 2019. URANSE simulation for the seakeeping of the KVLCC2 ship model in short and long regular head waves. In: IOP Conference Series: Materials Science and Engineering, Vol. 591, No. 1. IOP Publishing, 012102.
Benek, J., Steger, J., Dougherty, F., 1986. Chimera: A grid-embedding technique, vol. 85, no. 64, Arnold Engineering Development Center, Air Force Systems Command, United ....
Caretto, L., Gosman, A., Patankar, S., Spalding, D., 1973. Two calculation procedures for steady, three-dimensional flows with recirculation. In: Proceedings of the Third International Conference on Numerical Methods in Fluid Mechanics: Vol. II Problems of Fluid Mechanics. Springer, pp. 60–68.
Chang, M.-S., 1977. Computations of three-dimensional ship motions with forward speed. In: Proceedings of the 2nd International Conference on Numerical Ship Hydrodynamics. pp. 124–135.
Chen, H., Qian, L., Ma, Z., Bai, W., Li, Y., Causon, D., Mingham, C., 2019. Application of an overset mesh based numerical wave tank for modelling realistic free-surface hydrodynamic problems. Ocean Eng. 176, 97–117.
Chen, W., Warmink, J., Van Gent, M., Hulscher, S., 2021. Numerical modelling of wave overtopping at dikes using OpenFOAM®. Coast. Eng. 166, 103890.
Chowdhury, J.I., Faieq, A., Amin, O.M., 2023. Seakeeping analysis of a tanker with hard sail-based wind propulsion system in various seaways. Ocean Eng. 278, 114481.
Conde, J., 2019. Comparison of different methods for generation and absorption of water waves. Rev. Eng. Térmica 18 (1), 71–77.
Connell, K.O., Cashman, A., 2016. Development of a numerical wave tank with reduced discretization error. In: 2016 International Conference on Electrical, Electronics, and Optimization Techniques. ICEEOT, IEEE, pp. 3008–3012.
Crank, J., Nicolson, P., 1947. A practical method for numerical evaluation of solutions of partial differential equations of the heat-conduction type. Math. Proc. Cambridge Philos. Soc. 43 (1), 50–67.
Damián, S.M., Nigro, N.M., 2014. An extended mixture model for the simultaneous treatment of small-scale and large-scale interfaces. Internat. J. Numer. Methods Fluids 75 (8), 547–574.
De, S., 1955. Contributions to the theory of Stokes waves. Math. Proc. Cambridge Philos. Soc. 51 (4), 713–736.
Decorte, G., Lombaert, G., Monbaliu, J., 2019. A first assessment of the interdependency of mesh motion and free surface models in OpenFOAM regarding wave-structure interaction. In: MARINE VIII: Proceedings of the VIII International Conference on Computational Methods in Marine Engineering. CIMNE, pp. 795–806.

Deshpande, S.S., Anumolu, L., Trujillo, M.F., 2012. Evaluating the performance of the two-phase flow solver interfoam. Comput. Sci. Discov. 5 (1), 014016.

Devolder, B., Rauwoens, P., Troch, P., 2017. Application of a buoyancy-modified k-ω SST turbulence model to simulate wave run-up around a monopile subjected to regular waves using OpenFOAM®. Coast. Eng. 125, 81–94.

Dullweber, A., Leimkuhler, B., McLachlan, R., 1997. Symplectic splitting methods for rigid body molecular dynamics. J. Chem. Phys. 107 (15), 5840–5851.

el Moctar, B.O., Schellin, T.E., Söding, H., 2021. Numerical Methods for Seakeeping Problems. Springer.

Farmer, J., Martinelli, L., Jameson, A., 1994. Fast multigrid method for solving incompressible hydrodynamic problems with free surfaces. AIAA J. 32 (6), 1175–1182.

Gao, Q., Song, L., Yao, J., 2021. RANS prediction of wave-induced ship motions, and steady wave forces and moments in regular waves. J. Mar. Sci. Eng. 9 (12), 1459.

Garoosi, F., Mellado-Cusicahua, A.N., Shademani, M., Shakibaeinia, A., 2022. Experimental and numerical investigations of dam break flow over dry and wet beds. Int. J. Mech. Sci. 215, 106946.

Gingold, R.A., Monaghan, J.J., 1977. Smoothed particle hydrodynamics: theory and application to non-spherical stars. Mon. Not. R. Astron. Soc. 181 (3), 375–389.

Goda, Y., Suzuki, Y., 1976. Estimation of incident and reflected waves in random wave experiments. In: Coastal Engineering 1976. pp. 828–845.

Grasso, A., Villa, D., Brizzolara, S., Bruzzone, D., 2010. Nonlinear motions in head waves with a RANS and a potential code. J. Hydrodyn. 22 (1), 172–177.

Guevel, P., Bougis, J., 1982. Ship-motions with forward speed in infinite depth. Int. Shipbuild. Prog. 29 (332), 103–117.

Hänninen, S.K., Mikkola, T., Matusiak, J., 2012. On the numerical accuracy of the wave load distribution on a ship advancing in short and steep waves. J. Mar. Sci. Technol. 17, 125–138.

Higuera, P., Lara, J.L., Losada, I.J., 2013. Realistic wave generation and active wave absorption for Navier–Stokes models: Application to OpenFOAM®. Coast. Eng. 71, 102–118.

Hirt, C.W., Nichols, B.D., 1981. Volume of fluid (VOF) method for the dynamics of free boundaries. J. Comput. Phys. 39 (1), 201–225.

Hochbaum, A.C., Vogt, M., 2002. Towards the simulation of seakeeping and maneuvering based computation of the free surface viscous ship flow. In: Proceedings of the 24th Symposium on Naval Hydrodynamics. Fukuoka, Japan.

Huang, L., et al., 2022. A review on the modelling of wave-structure interactions based on OpenFOAM. OpenFOAM® J. 2, 116–142.

Inglis, R., Price, W., 1980. Hydrodynamic coefficients of an oscillating ellipsoid moving in the free surface. J. Hydronaut. 14 (4), 105–110.

Islam, H., Mohapatra, S., Gadelho, J., Soares, C.G., 2019. OpenFOAM analysis of the wave radiation by a box-type floating structure. Ocean Eng. 193, 106532.

Issa, R.I., 1986. Solution of the implicitly discretised fluid flow equations by operator-splitting. J. Comput. Phys. 62 (1), 40–65.

Jacobsen, N.G., Fuhrman, D.R., Fredsøe, J., 2012a. A wave generation toolbox for the open-source CFD library: OpenFoam®. Int. J. Numer. Methods Fluids 70 (9), 1073–1088. http://dx.doi.org/10.1002/fld.2726.

Jacobsen, N.G., Fuhrman, D.R., Fredsøe, J., 2012b. A wave generation toolbox for the open-source CFD library: OpenFoam®. Internat. J. Numer. Methods Fluids 70 (9), 1073–1088.

Jasak, H., 1996. Error Analysis and Estimation for the Finite Volume Method with Applications to Fluid Flows. Imperial College London (University of London).

Karola, A., Hirdaris, S., Matusiak, J., Mikkola, T., 2022. Wave loads and ship motions evaluated by linear strip and panel methods. In: International Conference on Offshore Mechanics and Arctic Engineering, Vol. 85895. American Society of Mechanical Engineers, V05AT06A043.

Karola, A., Tavakoli, S., Mikkola, T., Matusiak, J., Hirdaris, S., 2023. Absorption of wave reflections in way of an inlet boundary. In: IOP Conference Series: Materials Science and Engineering, Vol. 1288, No. 1. IOP Publishing, 012013.

Kim, S.P., 2011. CFD as a seakeeping tool for ship design. Int. J. Nav. Archit. Ocean Eng. 3 (1), 65–71.

Kodama, Y., 1985. Computation of 3-D incompressible Navier-Stokes equations for flow around a ship hull using an implicit factored method. In: Osaka International Colloquium on Ship Viscous Flow. Osaka.

Korvin-Kroukovsky, B.V., Jacobs, W.R., 1957. Pitching and heaving motions of a ship in regular waves. Trans. Sname 65, 590–632.

Koshizuka, S., Oka, Y., 1996. Moving-particle semi-implicit method for fragmentation of incompressible fluid. Nucl. Sci. Eng. 123 (3), 421–434.

Kukkanen, T., Matusiak, J., 2014. Nonlinear hull girder loads of a RoPax ship. Ocean Eng. 75, 1–14.

Lakshmynarayanana, P., Hirdaris, S., 2020. Comparison of nonlinear one-and two-way FFSI methods for the prediction of the symmetric response of a containership in waves. Ocean Eng. 203, 107179.

Larsen, B.E., Fuhrman, D.R., Roenby, J., 2019. Performance of interFoam on the simulation of progressive waves. Coast. Eng. J. 61 (3), 380–400.

Li, Y., Fuhrman, D.R., 2022. Computational fluid dynamics simulation of deep-water wave instabilities involving wave breaking. J. Offshore Mech. Arct. Eng. 144 (2), 021901.

Li, T., Matusiak, J., Lehtimäki, R., 2001. Numerical simulation of viscous flows with free surface around realistic hull forms with transom. Internat. J. Numer. Methods Fluids 37 (5), 601–624.

Liapis, S., 1985. Seakeeping computations using time-domain analysis. In: Procd. of the 4th International Conference on Numerical Ship Hydrodynamics. Washington DC.

Lin, P., 2008. Numerical Modeling of Water Waves. CRC Press.

Löhrmann, J., Hochbaum, A.C., 2014. Simulation of seakeeping tests using open-FOAM. In: Proceedings of the 17th Numerical Towing Tank Symposium.

Madsen, P., 1983. Wave reflection from a vertical permeable wave absorber. Coast. Eng. 7 (4), 381–396.

Mayer, S., Garapon, A., Sørensen, L.S., 1998. A fractional step method for unsteady free-surface flow with applications to non-linear wave dynamics. Internat. J. Numer. Methods Fluids 28 (2), 293–315.

Menter, F., Esch, T., 2001. Elements of industrial heat transfer predictions. In: 16th Brazilian Congress of Mechanical Engineering, Vol. 109. COBEM, p. 650.

Menter, F.R., Kuntz, M., Langtry, R., 2003. Ten years of industrial experience with the SST turbulence model. Turbul. Heat Mass Transfer 4 (1), 625–632.

Miyata, H., Nishimura, S., Masuko, A., 1985. Finite difference simulation of nonlinear waves generated by ships of arbitrary three-dimensional configuration. J. Comput. Phys. 60 (3), 391–436.

Morgan, G.C.J., Zang, J., Greaves, D., Heath, A., Whitlow, C., Young, J., 2011. Using the rasInterFoam CFD model for wave transformation and coastal modelling. Coast. Eng. Proc. (32), 23.

NASA, 2023. NASA langley turbulence model resource. https://turbmodels.larc.nasa.gov/sst.html. (Accessed 12 2023).

Newmark, N.M., 1959. A method of computation for structural dynamics. J. Eng. Mech. Div. 85 (3), 67–94.

Ohmori, T., 1998. Finite-volume simulation of flows about a ship in maneuvering motion. J. Mar. Sci. Technol. 3, 82–93.

OpenFOAM, 2023. Openfoam user guide. https://doc.openfoam.com/2212/. (Accessed 12 2023).

Orihara, H., Miyata, H., 2003. Evaluation of added resistance in regular incident waves by computational fluid dynamics motion simulation using an overlapping grid system. J. Mar. Sci. Technol. 8, 47–60.

Orlanski, I., 1976. A simple boundary condition for unbounded hyperbolic flows. J. Comput. Phys. 21 (3), 251–269.

Palm, J., Eskilsson, C., Paredes, G.M., Bergdahl, L., 2016. Coupled mooring analysis for floating wave energy converters using CFD: Formulation and validation. Int. J. Mar. Energy 16, 83–99.

Parunov, J., Soares, C.G., Hirdaris, S., Iijima, K., Wang, X., Brizzolara, S., Qiu, W., Mikulić, A., Wang, S., Abdelwahab, H., 2022. Benchmark study of global linear wave loads on a container ship with forward speed. Mar. Struct. 84, 103162.

Queutey, P., Visonneau, M., 2007. An interface capturing method for free-surface hydrodynamic flows. Comput. & Fluids 36 (9), 1481–1510.

Rakhsha, M., Kees, C.E., Negrut, D., 2021. Lagrangian vs. Eulerian: An analysis of two solution methods for free-surface flows and fluid solid interaction problems. Fluids 6 (12), 460.

Rhee, S.H., Stern, F., 2001. Unsteady RANS method for surface ship boundary layer and wake and wave field. Internat. J. Numer. Methods Fluids 37 (4), 445–478.

Rienecker, M.M., Fenton, J.D., 1981. A Fourier approximation method for steady water waves. J. Fluid Mech. 104, 119–137.

Rodríguez, M., Spinneken, J., 2016. A laboratory study on the loading and motion of a heaving box. J. Fluids Struct. 64, 107–126.

Roenby, J., Bredmose, H., Jasak, H., 2016. A computational method for sharp interface advection. R. Soc. Open Sci. 3 (11), 160405.

Roenby, J., Larsen, B.E., Bredmose, H., Jasak, H., 2017. A new volume-of-fluid method in OpenFOAM. In: MARINE VI: Proceedings of the VI International Conference on Computational Methods in Marine Engineering. CIMNE, pp. 266–277.

Salvesen, N., Tuck, E., Faltisen, O., 1970. Ship motions and sea loads. Trans. SNAME 78.

Sato, Y., Miyata, H., Sato, T., 1999. CFD simulation of 3-dimensional motion of a ship in waves: application to an advancing ship in regular heading waves. J. Mar. Sci. Technol. 4, 108–116.

Schmitt, P., Windt, C., Davidson, J., Ringwood, J.V., Whittaker, T., 2020. Beyond VoF: alternative OpenFOAM solvers for numerical wave tanks. J. Ocean Eng. Mar. Energy 6, 277–292.

Show, T.K., Hirdaris, S., Datta, R., et al., 2022. A fully coupled time-domain BEM-FEM method for the prediction of symmetric hydroelastic responses of ships with forward speed. Shock Vib. 2022.

Sulovsky, I., Hauteclocque, G.d., Greco, M., Prpić-Oršić, J., 2023. Comparative study of potential flow and CFD in the assessment of seakeeping and added resistance of ships. J. Mar. Sci. Eng. 11 (3), 641.

Tahara, Y., Stern, F., 1996. A large-domain approach for calculating ship boundary layers and wakes and wave fields for nonzero Froude number. J. Comput. Phys. 127 (2), 398–411.

Takada, N., Miyata, H., Sato, T., 1998. CFD simulation of 3-dimensional motion of a vehicle with movable wings application to the keel of a racing yacht. J. Soc. Nav. Archit. Japan 1998 (184), 37–45.

Tavakoli, S., Huang, L., Babanin, A.V., 2021. Drift motion of floating bodies under the action of green water. In: International Conference on Offshore Mechanics and Arctic Engineering, Vol. 85161. American Society of Mechanical Engineers, V006T06A013.

Tezdogan, T., Demirel, Y.K., Kellett, P., Khorasanchi, M., Incecik, A., Turan, O., 2015. Full-scale unsteady RANS CFD simulations of ship behaviour and performance in head seas due to slow steaming. Ocean Eng. 97, 186–206.

Vukčević, V., Jasak, H., Gatin, I., 2017. Implementation of the ghost fluid method for free surface flows in polyhedral finite volume framework. Comput. & Fluids 153, 1–19.

Weber, J., 2016. Numerical Investigation on the Damping of Water Waves in a Towing Tank (MSc thesis). Technical Univesity of Berlin, Berlin, Germany.

Wei, Y., Tezdogan, T., 2022. A fluid-structure interaction model on the hydroelastic analysis of a container ship using PRECICE. In: International Conference on Offshore Mechanics and Arctic Engineering, Vol. 85925. American Society of Mechanical Engineers, V007T08A035.

Weymouth, G.D., Wilson, R.V., Stern, F., 2005. RANS computational fluid dynamics predictions of pitch and heave ship motions in head seas. J. Ship Res. 49 (02), 80–97.

Windt, C., Davidson, J., Ransley, E.J., Greaves, D., Jakobsen, M., Kramer, M., Ringwood, J.V., 2020. Validation of a CFD-based numerical wave tank model for the power production assessment of the wavestar ocean wave energy converter. Renew. Energy 146, 2499–2516.

Windt, C., Davidson, J., Schmitt, P., Ringwood, J.V., 2019. On the assessment of numerical wave makers in CFD simulations. J. Mar. Sci. Eng. 7 (2), 47.

Yamamoto, Y., Fujino, M., Fukasawa, T., 1978. Motion and longitudinal strength of a ship in head sea and the effects of non-linearities. J. Soc. Nav. Archit. Japan 1978 (143), 179–187.

Yan, M., Ma, X., Bai, W., Lin, Z., Li, Y., 2020. Numerical simulation of wave interaction with payloads of different postures using OpenFOAM. J. Mar. Sci. Eng. 8 (6), 433.

Yan, J., Pan, D., Zhou, X., He, K., 2015. The prediction of ship motions and added resistance based on RANS. In: 2015 15th International Conference on Control, Automation and Systems. ICCAS, IEEE, pp. 1978–1982.

Yao, J., Cheng, X., Song, X., Zhan, C., Liu, Z., 2021. RANS computation of the mean forces and moments, and wave-induced six degrees of freedom motions for a ship moving obliquely in regular head and beam waves. J. Mar. Sci. Eng. 9 (11), 1176.